



Research
Green Chemical Engineering—Review

Catalyst Engineering for Electrochemical Energy Conversion from Water to Water: Water Electrolysis and the Hydrogen Fuel Cell

Lishan Peng, Zidong Wei*

Chongqing Key Laboratory of Chemical Process for Clean Energy and Resource Utilization, School of Chemistry and Chemical Engineering, Chongqing University, Chongqing 400044, China



ARTICLE INFO

Article history:

Received 21 January 2019

Revised 16 May 2019

Accepted 12 July 2019

Available online 22 May 2020

Keywords:

Renewable energy system
Hydrogen–water energy conversion
Electrocatalysis
Electrocatalyst engineering
Structure design
Water electrolysis
Fuel cell

ABSTRACT

In the context of the current serious problems related to energy demand and climate change, substantial progress has been made in developing a sustainable energy system. Electrochemical hydrogen–water conversion is an ideal energy system that can produce fuels via sustainable, fossil-free pathways. However, the energy conversion efficiency of two functioning technologies in this energy system—namely, water electrolysis and the fuel cell—still has great scope for improvement. This review analyzes the energy dissipation of water electrolysis and the fuel cell in the hydrogen–water energy system and discusses the key barriers in the hydrogen- and oxygen-involving reactions that occur on the catalyst surface. By means of the scaling relations between reactive intermediates and their apparent catalytic performance, this article summarizes the frameworks of the catalytic activity trends, providing insights into the design of highly active electrocatalysts for the involved reactions. A series of structural engineering methodologies (including nanoarchitecture, facet engineering, polymorph engineering, amorphization, defect engineering, element doping, interface engineering, and alloying) and their applications based on catalytic performance are then introduced, with an emphasis on the rational guidance from previous theoretical and experimental studies. The key scientific problems in the electrochemical hydrogen–water conversion system are outlined, and future directions are proposed for developing advanced catalysts for technologies with high energy-conversion efficiency.

© 2020 THE AUTHORS. Published by Elsevier LTD on behalf of Chinese Academy of Engineering and Higher Education Press Limited Company. This is an open access article under the CC BY-NC-ND license (<http://creativecommons.org/licenses/by-nc-nd/4.0/>).

1. Introduction

While worldwide energy consumption continues to grow, unfortunately, nearly 88% of the current energy economy relies on fossil fuels [1]. It is only a matter of time before fossil fuels become either completely depleted or unprofitable to retrieve. Despite their outsized share of the energy portfolio, the era of fossil fuels is coming to an end [2]. Apart from the problem of diminishing availability, the negative externalities of fossil fuels have posed a prominent risk to the global ecosystem. At present, the world's main source of energy is the combustion of fossil fuels. The byproducts of this combustion (e.g., CO₂, NO_x, SO_x, and fine particles) seriously pollute the air, soil, and water [3–5]. It is urgent that we adopt a fresh mindset in order to find solutions to these problems and to devise a future with a more secure and sustainable

energy supply. Renewable energy will play a vital role in the world's energy future. However, there is a market barrier that stems from a major difference between renewable and conventional energy sources [6–9]. The amount of energy (mainly in the form of electricity) yielded by renewable energy sources can change unpredictably over a short period of time. For example, solar systems only produce energy when the sun is shining. Unfortunately, other renewable sources such as wind and tidal movements also possess adverse inconstancy [10]. This inconstancy makes the current generation of renewable energy less reliable than fossil-fuel-derived energy, because its output is highly dependent on weather conditions (i.e., clouds or wind) and time (i.e., day or night). For renewable energy to be practical on a very large scale, highly efficient electricity conversion and the high-density storage of electricity are required to enable energy-distribution technologies.

Electrochemical hydrogen–water conversion (H₂ + O₂ ↔ H₂O) is a clean and efficient execute solution for a sustainable energy system [11,12]. To be specific, renewable energy can be converted

* Corresponding author.

E-mail address: zdwei@cqu.edu.cn (Z. Wei).

into chemical energy stored in hydrogen (H_2) through water electrolysis [13]. Inversely, hydrogen molecules can be electrochemically recombined into water (H_2O) in order to output electricity through fuel cells. In this energy system, hydrogen acts as the energy carrier, and the energy conversion is independent of thermal cycles [1,14,15]. Because it is based on electrochemical reactions, hydrogen–water conversion can drastically reduce the release of climate-changing gases and compounds that are harmful to the natural environment and to human health. However, for the purposes of practical application, hydrogen must first be obtained, then be stored, and finally be converted back to water to release the stored energy [16]. In order to achieve this target, efficient, low-cost water electrolysis and fuel cell technology must be efficiently integrated together. Electrochemical processes are the core of these energy conversion technologies, including the hydrogen evolution reaction (HER) and the oxygen evolution reaction (OER) in the water electrolyzer, and the oxygen reduction reaction (ORR) and the hydrogen oxidation reaction (HOR) in the hydrogen–oxygen fuel cell [17,18]. The output performance of the aforementioned energy conversion technologies is significantly influenced by the efficiency of these four electrochemical reactions. Thus, the most critical problem in this sustainable energy system is how to effectively catalyze these reactions on the catalytic electrode surface in order to attain the lowest overpotential and highest current density [19–22]. Apart from the potential drop induced by electrochemical reactions, the electrical resistances and transport-related resistances affect the overall cell voltage of the water electrolysis and fuel cell. Accelerating the electron and proton transfer and the product emission by optimizing the electrode structure is another problem that requires extensive attention.

This article provides a comprehensive review of recent advances toward the structural engineering of electrocatalytic catalysts for electrochemical hydrogen–water conversion. Two major issues are addressed in this review: ① the origin of energy dissipation in the electrochemical hydrogen–water conversion system; and ② the structural design of electrocatalysts for high energy-conversion efficiency, driven by the combination of fundamental science and practical technology. In the second section, after a brief introduction of the electrochemical process that occurs in hydrogen–water conversion, we present a review of the energy dissipation in the two functioning technologies—that is, water electrolysis and the fuel cell—from a practical standpoint, and use classical kinetics to analyze the key barrier of the electrochemical reactions occurring on the catalyst surface. With the aid of scaling relations among reactive intermediates, we develop a framework to understand catalytic trends, which ultimately provides rational guidance toward the development of improved catalysts for a wide range of reactions. In the third section, we summarize general strategies for designing higher-performance electrocatalysts and discuss their advantages and drawbacks. Featured examples of state-of-the-art electrocatalysts that have been achieved for each reaction by structural design are presented in this part, demonstrating the successful combination of synthetic chemistry, electrocatalytic chemistry, and computational chemistry. The last section outlines the key scientific problems in the electrochemical hydrogen–water conversion system and provides further development direction for catalyst design for a renewable and clean energy system with a high energy efficiency.

2. Fundamentals of electrocatalysis

2.1. Electrochemical reactions of hydrogen–water conversion

As illustrated in Fig. 1, two different functioning technologies are involved in this renewable and clean energy system: water

electrolysis and the fuel cell. The two electrolyzers are mainly composed of four parts: the electrolyte (e.g., H_2O), the ion-exchange membrane (e.g., a Nafion membrane), the anode electrode, and the cathode electrode [23,24]. In order to accelerate water splitting, the two electrodes are always coated with a highly active and stable catalyst layer. In the water electrolyzer, electrical energy is consumed to split water into gaseous hydrogen (H_2) and oxygen (O_2). Taking acid water electrolysis as an example, water is oxidized to form oxygen molecules and protons at the anode, as the electrons pass through the external circuit and the protons pass through the membrane down to the cathode. Meanwhile, the protons and electrons combine at the cathode to form hydrogen molecules.

The electrochemical reaction that occurs in the fuel cell is the exact opposite of the water electrolysis process [25]. A spontaneous “cold” combustion of hydrogen and oxygen occurs in the fuel cell device, in which hydrogen acts as the fuel and oxygen acts as the oxidizer. In general, hydrogen diffuses to the anode surface by penetrating through the electrode pores. Through the catalytic action of the catalyst layer, the adsorbed hydrogen is ionized and releases an electron at the electrode. Next, the hydrogen ions that pass through the electrolyte and the electrons that pass through the external circuit all reach the cathode, recombine with oxygen molecules to form water molecules, and release electricity. The heat generated by the internal reaction and electrical resistance can be removed by applying suitable water or air cooling systems. Table 1 summarizes the half-cell reactions of water electrolysis and the fuel cell in different media. The four reactions can be grouped into two reversible reaction couples: hydrogen-involving HER and HOR with an equilibrium potential (U_0) of 0 V versus reversible hydrogen electrode (vs RHE); and oxygen-involving ORR and OER with a U_0 of 1.23 V vs RHE. From a chemical point of view, hydrogen–water conversion is composed of two redox couples: The water/oxygen couple at high potential and the water/hydrogen couple at relatively low potential [26]. In acidic media, hydrated protons transfer charges from the anode to the cathode, while hydroxide ions act as charge carriers from the cathode to the anode in alkaline electrolytes.

2.2. Energy dissipation of water electrolysis and the fuel cell

According to the thermodynamics of hydrogen–water conversion, reversible water electrolysis and the H_2 – O_2 fuel cell have the same electrical onset potential of 1.23 V under standard conditions. However, the actual onset potential for the two reactions is far from the standard electrical potential. Under practical operating conditions, the cell voltage of the H_2 – O_2 fuel cell and of water electrolysis is always below 0.9 V and higher than 1.8 V, respectively, even utilizing state-of-the-art noble metals as the electrocatalysts [2,27–29]. In practice, in order to drive the electrochemical reaction process, there are a number of barriers that must be overcome, including the electrical resistance of the circuit, activation energies of the electrochemical reactions, blockage of the electrode surfaces by the product gas bubbles and water, and ionic transfer resistances across the electrolyte solution [24]. These barriers, which require a sufficient electrical energy supply, greatly reduce the energy conversion efficiency and cause the work potential to fall short of the thermodynamic potential, which is the so-called phenomenon of polarization (or overpotential, or overvoltage) [30]. Fig. 2 shows the resistances (i.e., the barriers) in a typical cell with a liquid electrolyte [31,32]. The first resistance from both ends (R_{Ω}^a and R_{Ω}^c) is the external electrical circuit resistance, which includes the internal resistance of the wiring and connections at the anode and cathode, and the resistance of the electrons across the catalyst layers, which are not always good electronic conductors [33]. R_{ct}^a and R_{ct}^c originate from the overpotential of the half-cell reactions

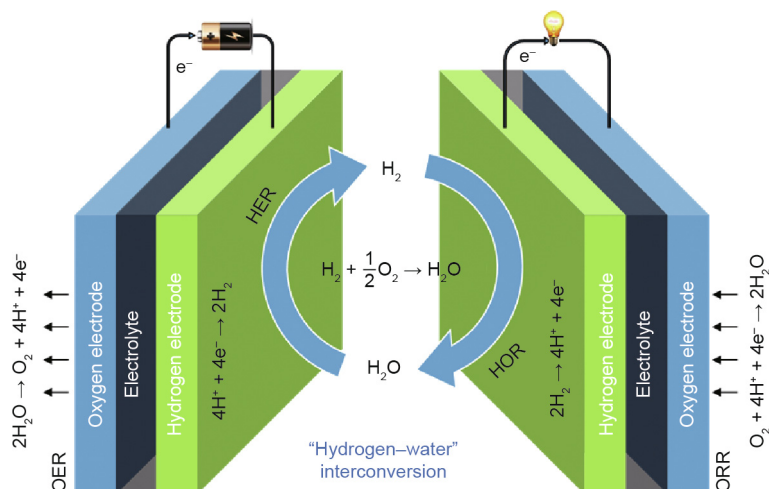


Fig. 1. Schematic illustration of water electrolysis and the fuel cell reactions in hydrogen–water electrochemical conversion.

Table 1

Summary of the half-cell reactions of water splitting and the fuel cell in acid and alkaline electrolyte.

Electrolyte	Water electrolysis	Fuel cell
Acidic solution	Cathode: $2\text{H}^+ + 2\text{e}^- \rightarrow \text{H}_2$ (0 V) Anode: $\text{H}_2\text{O} \rightarrow 2\text{H}^+ + \frac{1}{2}\text{O}_2 + 2\text{e}^-$ (1.23 V)	Cathode: $\text{H}_2 \rightarrow 2\text{H}^+ + 2\text{e}^-$ (0 V) Anode: $2\text{H}^+ + \frac{1}{2}\text{O}_2 + 2\text{e}^- \rightarrow \text{H}_2\text{O}$ (1.23 V)
Alkaline solution	Cathode: $2\text{H}_2\text{O} + 2\text{e}^- \rightarrow \text{H}_2 + 2\text{OH}^-$ (0 V) Anode: $2\text{OH}^- \rightarrow \text{H}_2\text{O} + \frac{1}{2}\text{O}_2 + 2\text{e}^-$ (1.23 V)	Cathode: $\text{H}_2 + 2\text{OH}^- \rightarrow 2\text{H}_2\text{O} + 2\text{e}^-$ (0 V) Anode: $\text{H}_2\text{O} + \frac{1}{2}\text{O}_2 + 2\text{e}^- \rightarrow 2\text{OH}^-$ (1.23 V)

on the surface of the anode [34]. R_D^O and R_D^H are caused by the diffusion layers close to the electrode surface when mass transport phenomena are involved or gaseous species are formed [35]. As for water electrolysis, the partial coverage of the electrode surface by generated bubbles hinders the contact between the electrode and electrolyte. Similarly, the product water acts as a blockage between the electrode and the H_2 and O_2 input, inducing a resistance of mass transport in an alkaline fuel cell (AFC). R_{ions} originates from the transport of ions in the electrolyte and R_{sep} stems from the resistance of the cell separator [36]. A similar situation is found in other types of cells, such as zero-gap and proton-exchange membrane (PEM) cells [37,38].

The resistances in cell systems can be classified into three categories: activation resistances (losses due to electrochemical reactions), ohmic resistances (losses due to ionic and electronic conduction), and concentration resistances (losses due to mass transport). Each of the three major losses contributes to the characteristic shape of the current–voltage (i – V) curve of the electrochemical cell [39,40]. Fig. 3 shows a typical i – V curve for water electrolysis and for a fuel cell. In the case of water electrolysis (Fig. 3(a)), the current starts to flow across the cell above the thermodynamic electrolysis voltage of 1.23 V. Additional voltage is required to overcome the resistances discussed above. At low current densities, the voltage drops caused by ohmic resistances are small, and the reaction activation overvoltage accounts for the dominant part of the voltage drop. The logarithmic shape of the polarization curve (the Tafel area) is attributed to the charge transfer phenomena at the anode and cathode. As the overvoltage increases further, the reaction activation barrier decreases, and the shape of the polarization curve becomes linear. This linear shape indicates that the ohmic resistance is now the key kinetic parameter of the cell. In the case of the fuel cell (Fig. 3(b)), the activation resistances mostly affect the initial part of the curve, the ohmic resistances are mainly apparent in the middle section of the curve, and the concentration resistances are significant in the

tail. Although the reactions that occur in the two functioning technologies are reversible, the shapes of the i – V curves are not the same: the i – V curve for water electrolysis generally obeys the Butler–Volmer model even at very high overpotentials, while the i – V curve for a fuel cell tends to show a constant value at high overpotentials due to the limitation in the mass transfer rate.

To improve the energy efficiency of the two electrochemical cells and thus improve the performance of the energy system, an understanding of these resistances must be grasped in order to minimize them. Ohmic losses are caused by the electrode material's resistance to the electron flow and the electrolyte's resistance to the ion flow; these can be reduced by utilizing highly conductive materials as the wiring and electrode substrate, and by diminishing the distance between the two electrodes [41–43]. The concentration losses, which are attributed to mass transport, can be relieved by increasing the pressure of the gaseous reactants or the concentration of the liquid electrolyte [44,45]. The two kinds of voltage drops mainly depend on the cell design and operation conditions. In addition to the above two resistances, the majority (> 60%) of the voltage drop in an electrochemical cell is induced by the Gibbs free-energy change for the endergonic transformation of the half-cell reactions [39]. Depending on the direction of the reactions, the activation polarizations greatly increase or decrease the anode voltage where the oxidation reaction takes place, and decrease or increase the cathode voltage where the reduction reaction occurs.

In electrochemistry, the Butler–Volmer relationship is used as the primary departure point to relate the overvoltage η across a metal–electrolyte interface to the current density j (in $\text{A}\cdot\text{cm}^{-2}$) across this interface [46]:

$$j = j_0 \left[e^{2nF\eta/(RT)} - e^{-(1-\alpha)nF\eta/(RT)} \right] \quad (1)$$

where η is the overvoltage—that is, the difference between the actual voltage across the interface and the equilibrium voltage; j_0

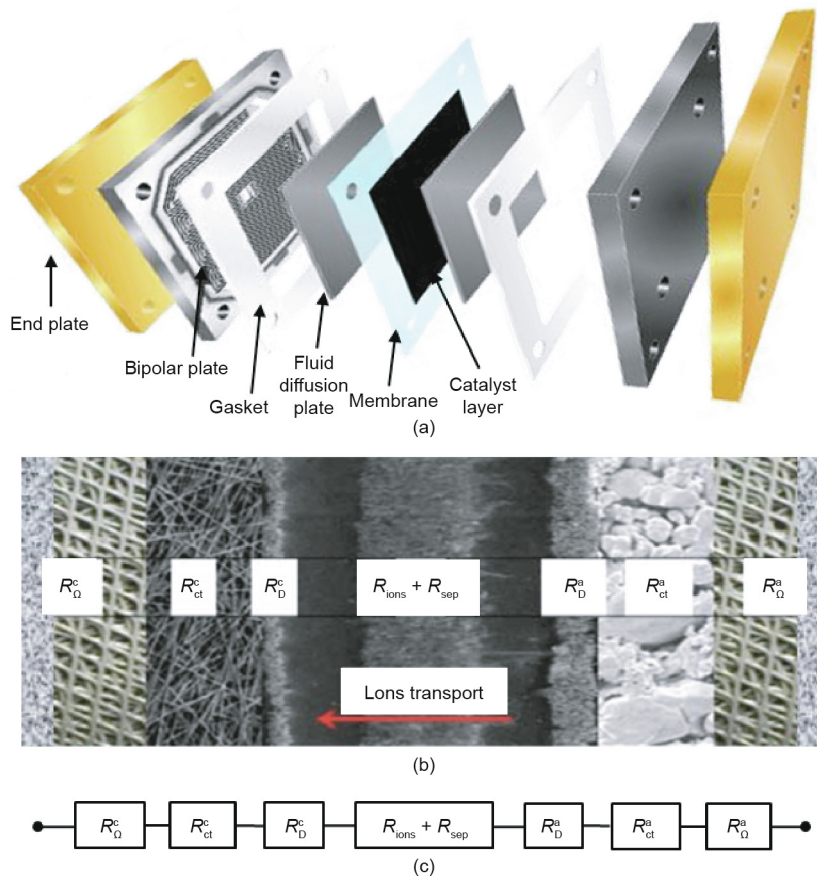


Fig. 2. (a) Schematic of a typical AFC with a liquid electrolyte; (b) cross-section of the electrolyzer; (c) equivalent electric circuit. Reproduced from Ref. [31] with the permission of Elsevier, ©2014.

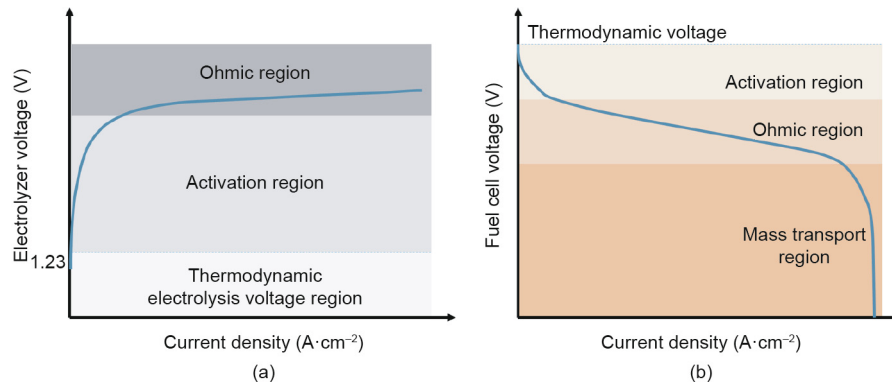


Fig. 3. Schematics of the polarization curves for (a) water electrolysis and (b) a fuel cell.

is the exchange current density in $\text{A}\cdot\text{cm}^{-2}$; α is the coefficient of the charge transfer; n is the number of electrons transferred in the electrochemical reaction; $F \approx 96\,485 \text{ C}\cdot\text{mol}^{-1}$ is the Faraday constant; R is the constant of a perfect gas ($0.082 \text{ J}\cdot(\text{K}\cdot\text{mol})^{-1}$); and T is the absolute temperature in K . The Butler–Volmer equation basically reveals that the current produced by an electrochemical reaction increases exponentially with the activation overvoltage and exchange current density. In fact, improving the reaction energy efficiency focuses on increasing j_0 , which represents the “rate of exchange” between the reactant and product at equilibrium. Taking the forward reaction for simplicity and including the concentration effects, j_0 is defined as follows:

$$j_0 = nFcf e^{-\Delta G_{\text{act}}/(RT)} \quad (2)$$

where c is the reactant surface concentration, f is the decay rate to products, and ΔG_{act} is the activation energy barrier for the forward reaction. Eq. (2) clearly shows that decreasing the size of the activation energy barrier (ΔG_{act}) will increase j_0 under a given environmental condition. In the actual reaction, only species in the activated state can undergo the transition from reactant to product. In fact, the activation energy of the reactions is strongly influenced by the electrode material [47]. A catalytic electrode is a site for species activation and transition. Using a highly catalytic electrode can significantly lower the activation barrier for the reaction, and

therefore provides a way to dramatically increase j_0 . To reduce the activation energy of the electrode reactions, continuing research efforts are focusing on the design of efficient catalytic electrode materials based on an understanding of the relationship between the activation energies, electrode materials, and surface configurations.

2.3. A guide for electrocatalyst design for hydrogen–water conversion

In terms of the reaction mechanism, the activation energy barrier (ΔG_{act}) can be quantified by the Gibbs free-energy change (ΔG_{max}) for the rate-determining step (RDS) at the equilibrium potential, and its theoretical value on different catalytic materials can be calculated by means of density functional theory (DFT) calculation. In this way, the relationship between the activation energy and the electrode material is built, as a volcano-shaped plot is obtained by plotting j_0 versus ΔG_{max} . The most common shape of the volcano plot is the HER rate description based on the Langmuir type of adsorption with the maximum located near the position where the hydrogen adsorption free energy (ΔG_{H^*}) is zero [48]. In the HER, the reaction species is first adsorbed on the catalyst surface to form the reaction intermediate ($\text{M}-\text{H}_{\text{ads}}$). After the aforementioned Volmer step, hydrogen molecules can be formed by the coupling of an electron and a proton in the electrolyte through a Heyrovsky step, or their direct combination via a Tafel step [30,49,50]. As a result, the ΔG_{H^*} is the overall decisive rate for HER [51,52]. In recent years, the DFT-calculated ΔG_{H^*} has been widely used as the activity descriptor [53–55], for many traditional metals, metal composites/metal alloys, and nonmetallic materials. As shown in Fig. 4(a), different metals show significant differences

in HER exchange current density, and the highly active metals (e.g., Pt) located near the top of the volcano plot possess optimal ΔG_{H^*} [56]. If the catalytic material has a weak adsorption force on hydrogen, the hydrogen atom can barely be absorbed on the surface of the material, and the overall reaction rate is determined by the adsorption step of hydrogen (Volmer step). On the other hand, a too-strong adsorption of hydrogen atoms onto catalytic materials results in difficulty breaking the $\text{M}-\text{H}_{\text{ads}}$ bond to form H_2 , and the RDS is the desorption step (Heyrovsky/Tafel). As the reverse process of HER, the RDS of HOR is the dissociative adsorption of H_2 on the catalyst surface, which involves electron transfer from the surface to the σ^* antibonding orbital of the H_2 molecule [57]. Consequently, the interaction of $\text{M}-\text{H}_{\text{ads}}$ also plays a dominant role in the kinetics of HOR, and the activity of HOR follows the same trend as HER on noble metal surfaces due to the high reversibility of these two reactions (Fig. 4(b)) [58–61].

In addition to the hydrogen-involved reactions, the relationship between j_0 and ΔG_{max} can be applied to the oxygen-related reactions that occur in hydrogen–water conversion. As shown in Figs. 4(c) and (d), the shapes of volcano plots for these reactions are quite similar, except for the reaction intermediates determining the reaction rate. In general, the ORR includes either a four-electron pathway to reduce oxygen to water, which is attractive for fuel cells, or a two-electron pathway, which is desirable for producing hydrogen peroxide [62]. In fact, a direct four-electron mechanism can either be a dissociative or associative process, depending on the oxygen dissociation barrier on the catalyst surface [63]. As a result, the oxygen adsorption strength (ΔG_{O^*}) is associated with the ORR activity to construct a volcano plot

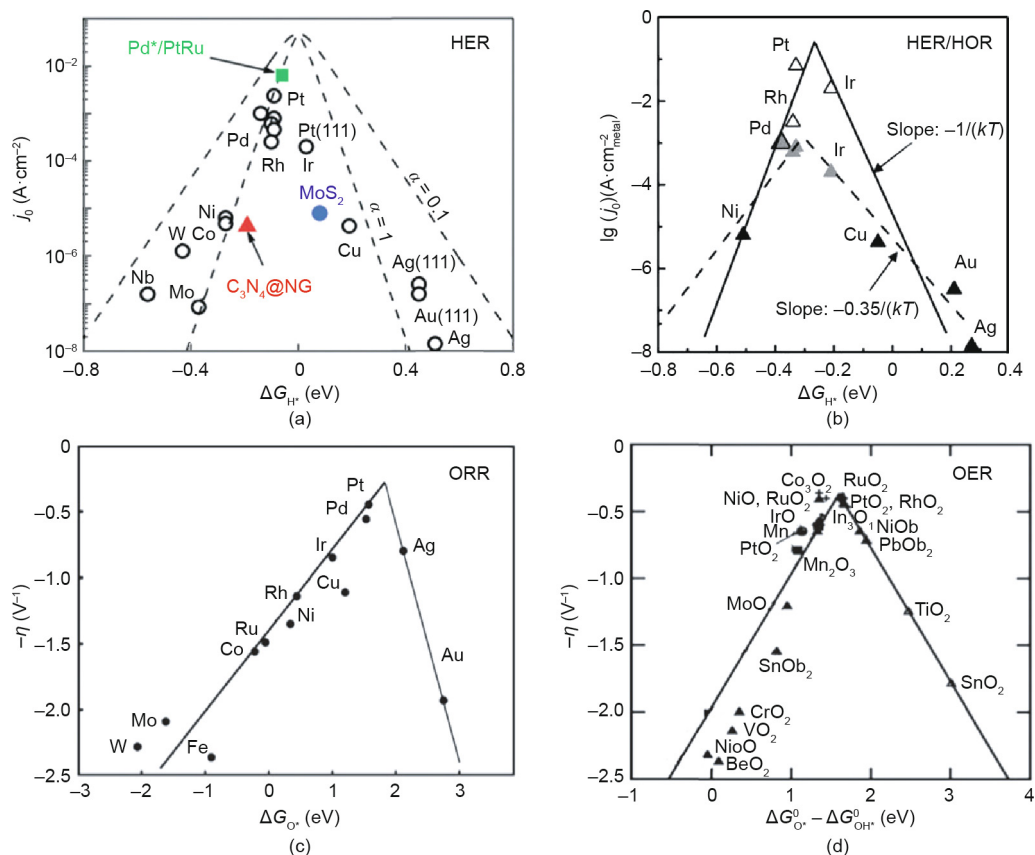


Fig. 4. (a) HER exchange current densities (j_0) as a function of ΔG_{H^*} for the surfaces of various materials; (b) volcano plot computing the ΔG_{H^*} as a function of the surface normalized HER/HOR exchange current densities (j_0) measured in acid electrolytes; (c) ORR activity for various metals vs ΔG_{O^*} ; (d) OER activity (overpotential at a certain value of current density) plotted against $\Delta G_{\text{O}^*} - \Delta G_{\text{OH}^*}$ for oxides. NG: nitrogen doped graphene. (a) Reproduced from Ref. [56] with permission of ACS Publications, ©2012; (b) reproduced from Ref. [61] with permission of IOP Publishing, ©2014; (c) reproduced from Ref. [63] with permission of ACS Publications, ©2004; (d) reproduced from Ref. [70] with permission of WILEY-VCH Verlag GmbH & Co. KGaA, ©2004.

(Fig. 4(c)) [63,64]. For metals that bind oxygen too strongly, the reaction rate is limited by the removal of O^* or OH^* species. For metals that bind oxygen too weakly, the reaction rate is limited by splitting of the $O-O$ bond in O_2 (dissociative mechanism) or, more likely, by the transfer of electrons and protons to the adsorbed O_2 (associative mechanism), depending on the applied potential [63]. As indicated by the volcano plot in Fig. 4(c), there seems to be some room for improvement, as even platinum (Pt) is not at the absolute peak. Metals with a somewhat lower oxygen-binding energy than Pt should have a higher ORR activity. Based on the above thermodynamic volcano plot, Viswanathan et al. [65] and Hansen et al. [66] developed a microkinetic model for ORR given that the OH binding energy is varying. They found a kinetic activity volcano that is in close agreement with the thermodynamic activity volcano, and identified an activity optimum at a 0.1 eV weaker O^* binding than Pt(111) for the reduction of O_2 to H_2O through a four-electron pathway.

The OER volcano plot has a long history starting in 1984, when Trasatti used the transition enthalpy from the lower to higher oxidation state of metal in metal oxides as a descriptor for the OER electrocatalytic activity of oxide electrodes [67]. That pioneering work viewed the OER process as a transition between two different configurations of the surface coordination complex. Accordingly, all metal oxides that are difficult or easy to oxidize are not very active for the OER. Difficult oxidization means that the intermediates are weakly adsorbed; therefore, water dissociation is the RDS. On the other hand, easy oxidization indicates that the intermediates are strongly adsorbed, and the removal of the O^* or OH^* species is the RDS. In this case, the OER reactivity has been related to the oxygen adsorption free energy ΔG_{O^*} [68,69], as in the case of ORR. However, the single descriptor of ΔG_{O^*} for OER activity is incomplete, as the four-electron OER involves multiple intermediates (OOH^* , OH^* , and O^*), the binding energies of which are strongly correlated and can hardly be decoupled [63,70]. A linear scaling relation exists between the binding energies of the different surface intermediates [70]; that is, if the energy associated with one reaction step is changed, the energies of the others also change. Thus, Man et al. [70] took the difference between the energy states of two subsequent intermediates ($\Delta G_{O^*} - \Delta G_{OH^*}$) as a descriptor for the catalytic activity of several compounds, including rutile, perovskite, spinel, rock salt, and bixbyite oxides (Fig. 4(d)), whose activity obeys the volcano plot quite well. In fact, the binding energies of OH^* and OOH^* (whether in OER or ORR) are related to each other by a constant energy value of approximately 3.2 eV in broad classes of metal oxide materials, regardless of the binding site [70,71]. As a result of this non-ideal scaling between OOH^* and OH^* , a real catalyst generally shows a minimum theoretical overpotential of 0.3–0.4 V [63,72,73], even for materials at the top of the OER and ORR volcano plots, including the extensively studied RuO_2 for OER [70] and Pt-based catalysts for ORR [74].

It is noticeable that the volcano plot appropriately demonstrates the Sabatier principle [75]; that is, an ideal catalyst should bind the reaction intermediates neither too weakly nor too strongly. In other words, optimal catalytic activity can be achieved using a catalyst surface with appropriate binding energies for reactive intermediates. To be specific, the best approximation to an ideal HER/HOR catalyst would be a material that is capable of minimizing the absolute value of ΔG_{H^*} , and the ideal ORR and OER catalysts would be able to optimize the ΔG_{O^*} and $\Delta G_{O^*} - \Delta G_{OH^*}$, respectively. In fact, aside from decreasing the activation barrier, there is another significant way to increase j_0 , which is not apparent from Eq. (2): that is, to increase the number of possible reaction sites per unit area [76–79]. j_0 represents the current density, or the reaction current per unit area, and the area for current density is generally based on the projected geometric area of

an electrode. The true electrode surface area of an electrode with an extremely rough surface can be orders of magnitude greater than the geometric electrode area, and can thus provide many more reaction sites. Therefore, the effective j_0 of a rough electrode surface will be greater than that of a smooth electrode surface. Another simple way to increase the density of active sites is to enlarge the amount of catalyst on a given electrode. However, an excessive amount of catalyst will hinder the charge and proton transfer on the electrode surface. As a result, the activity of the electrode does not increase linearly with the amount of catalyst.

In conclusion, there are two general methods for increasing the activity (or rate of reaction) of an electrocatalyst system: ① improving the intrinsic activity of each active site; and ② increasing the density of active sites on a given electrode. Both methods have pros and cons. The difference in intrinsic activity between different catalysts may be more than ten orders of magnitude, while the difference in activity caused by catalyst loading will be only 1–3 orders of magnitude. Improving the intrinsic activity of each active site is the most fundamental and effective way to achieve high activity, and its realization must be based on a deep understanding of the reaction mechanism and material properties. Increasing the number of active sites is an easier strategy, but the activity growth is limited. At the same time, activity promotion by increasing catalyst loading is obtained through the sacrifice of increasing the electrode cost and the charge and proton transfer blockage. In practice, the two methods are not mutually exclusive and can ideally be implemented simultaneously, thus greatly enhancing the activity of catalyst.

3. Materials design for electrochemical hydrogen–water conversion

3.1. Nanoarchitecture

It is well known that the current density of a catalyst increases as the density of the active sites increases. Exposing more active sites is important in achieving high catalytic performance. Nanoarchitecture has been considered to be the most effective strategy, as it allows the density of active sites to be directly enriched and utilized, and thus efficiently optimizes the electrocatalytic activity [80–84]. The relation between the actual active surface area and the overall performance of an electrocatalyst was first recognized in transition-metal alloy systems. As early as 1982, Brown et al. [85] found that an alloy surface is generally rougher than that of a single metal, and can provide more active sites for a catalytic reaction. With the aid of nanostructuring and selective etching of molybdenum (Mo) in Ni–Mo alloys [85–87], the surface area of Ni–Mo alloys greatly increased, resulting in an obvious improvement in catalytic reactivity. With the rapid development of synthesis techniques, a series of electrocatalytic nanomaterials with different morphologies have been achieved in the past decade, including nanocages, nanofibers, nanoflowers, nano-foam, nanonets, nano-needles, nano-rings, nano-shells, and nanowires [77,88–91]. Faber et al. [92] reported metallic cobalt disulfide (CoS_2) as a highly active catalyst for HER, and demonstrated the crucial role of geometric structure in determining its overall catalytic performance. Compared with the common morphologies of nanoparticles and nanofilm, an increase in active surface area drastically improves the HER catalytic performance of microstructured and nanostructured electrodes (Fig. 5), endowing the CoS_2 nanowire electrodes with overpotentials as low as 145 mV for driving a current density of $-10 \text{ mA}\cdot\text{cm}^{-2}$. In addition, nanostructuring possesses a dual function in terms of both operational stability and reaction rate through the facilitation of mass transport and

the removal of generated gas bubbles or water from the catalyst surface. Our group synthesized Mo₂C/C with a two-dimensional (2D) lamellar structure via a controllable synthesis using a self-assembly and pre-shaping strategy [93]. The highly dispersed Mo₂C nanoparticles and the 2D lamellar structure effectively boosted the mass and charge transfer across the Mo₂C active sites, facilitating the electrochemical HER process. Moreover, our group further synthesized a series of three-dimensional (3D) nanostructured catalytic materials, including the NiCo₂(SOH)_x nanoflower [94], the coral-like FeNi(OH)_x [95], the Ni-VC nanobosage [96], Ni-Mo₂C nanowire [97], and the Ni(OH)₂@Ni₂P nanopillar [98]. All these materials possessed highly active surfaces, fast electron transfer, and gas escape channels, which are beneficial for catalyzing water electrolysis.

To be specific, a rapid loss resulting from water flooding may take place in ORR catalysts, apart from deactivation during a long operation time [99,100]. Water flooding will interrupt the O₂ supply to active sites as the porous channels are obstructed by the accumulation of water, resulting in the termination of ORR in the flooded region [101,102]. In order to quantify the mass transfer and anti-flooding performance with the pore characteristics of electrocatalysts in a fuel cell, Wang et al. [103] designed a special “rattle-drum”-like work electrode for ORR catalysts. Benefiting from a bigger pore volume and regular pore arrangement, the

dual-porosity Pt/C catalyst exhibited four times the quantified mass transfer and anti-flooding efficiency of a commercial catalyst. In fact, different types of pores have special functions in the ORR process. Mesopores and macropores may be significant in mass transport during the ORR process [104–106], while micropores are beneficial for hosting most catalytic sites [107,108]. With the purpose of constructing hierarchically porous structures, the sacrificial template method has been widely adopted, using silica colloid [105,109–111], ordered mesoporous silica [106,112–114], polystyrene microspheres [115], and some other oxides [116,117] as templates. For example, a colloidal silica template was used by Liang et al. [118] for the synthesis of N-doped carbon catalyst with a high specific surface area of 1280 m²·g⁻¹, a hierarchically porous structure with meso/micropore distribution. However, the subsequent removal of the template can be time consuming and usually requires the usage of a strong acid or alkaline solution, which is dangerous to researchers and harmful to the environment. To avoid these disadvantages, our group developed a morphology-controlled approach using NaCl as the template, in which the template can be removed using hot water and then recycled [119–122]. A nanostructured polyaniline (PANI) with a special structure was encapsulated in the NaCl crystal via salt recrystallization, and then accurately converted into a carbon nanomaterial under high temperature (Fig. 6). Moreover, a mass of pores was created in

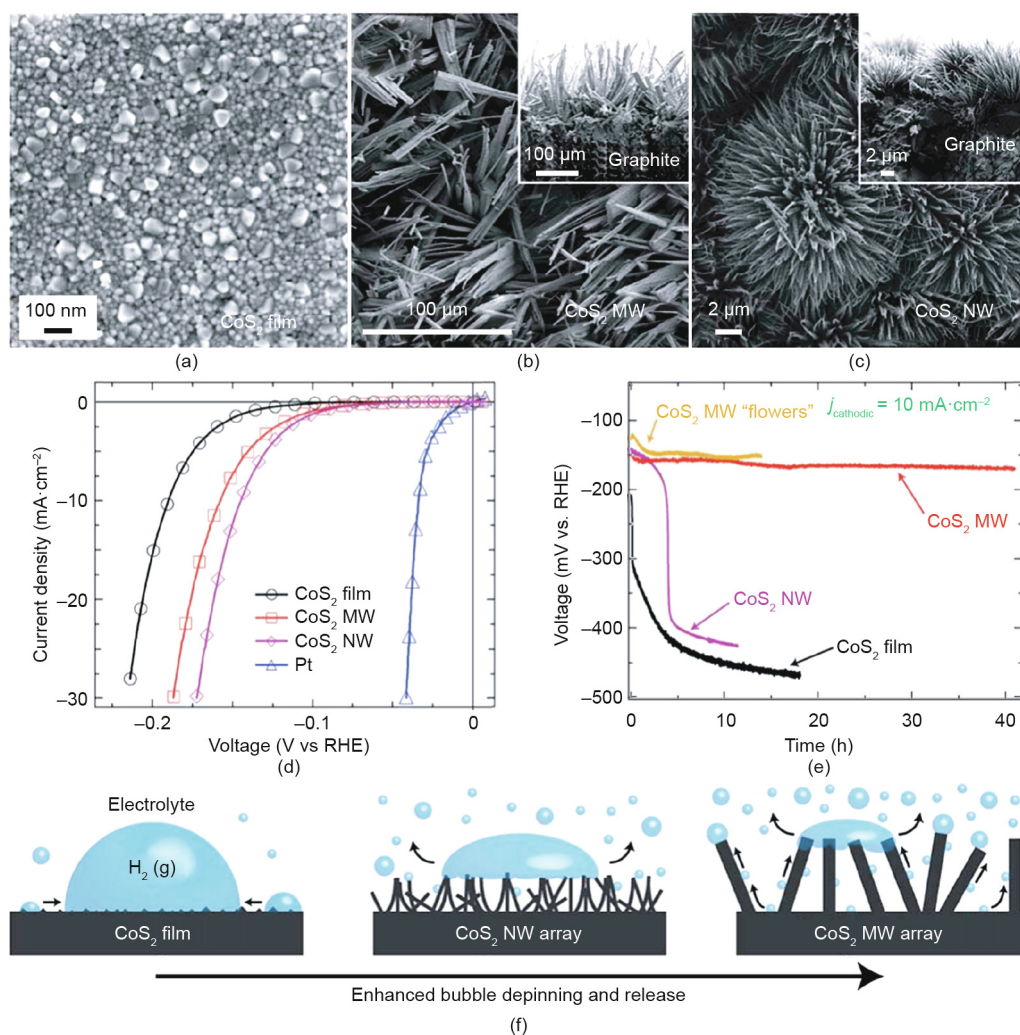


Fig. 5. (a–c) Scanning electron microscope (SEM) images of CoS₂ with different morphology; (d) electrochemical characterization and (e) long-term stability measurements of CoS₂ electrodes; (f) schematics of hydrogen gas bubble release from CoS₂ with different structures. MW: microwire; NW: nanowire. Reproduced from Ref. [92] with permission of ACS Publications, ©2014.

the carbon nanomaterial by gasification in a closed nanoreactor. Due to the multiple types of pores and high utilization of active sites, the 3D Fe/N–C catalysts exhibited excellent catalytic performance toward the ORR.

3.2. Facet engineering

Facet engineering is another widely studied method to modulate the catalytic performance of materials for a given reaction. The reactivity of catalytic materials is highly related to their exposed facets because the adsorption strength of the intermediate species of the catalytic reaction varies greatly on different surface facets of the catalyst. Facets are always denoted by Miller indices. The exposed facet(s) of a nanomaterial strongly correlate to the shape of the nanoparticle [123,124]. In general, faceted nanomaterials can be categorized into low-index and high-index faceted types [125]. Low-index facets are those for which the sum of the three components of the Miller indices (hkl) is small, whereas a high-index facet contains at least one Miller index greater than unity.

The structural sensitivity of the reactivity of low-index faceted nanomaterials has been demonstrated with regard to single-crystal Pt for HER. The surface morphology of Pt(hkl) with well-defined surfaces was confirmed by scanning tunneling microscopy (STM, Fig. 7), and the degree of activity was observed to follow the order $(110) > (100) > (111)$ in alkaline solution [126]. Importantly,

the activity in alkaline and acid electrolyte was found to differ substantially [127–129]. This pH effect involved structure–function relationships in the HER, and was further studied by Strmcnik et al. [130] with a focus on both Pt(111) and Pt(111) modified by Pt islands. Compared with the HER activity of the pristine Pt(111) surface, the HER on the Pt islands/Pt(111) electrode was found to be 5–6 times more active in alkaline solution, but only 1.5 times more active in acid electrolyte. The effect of pH on HER activity was shown to be due to the special ability of edge-step sites to dissociate water [131–135]. In addition, the activity order of Pt(hkl) is in line with the density of low-coordinated Pt atoms due to the accelerated water dissociation step on their metal surfaces [136–139].

A similar phenomenon was observed in the case of ORR activity on single-crystal Pt surfaces following a descending order in non-adsorbing HClO₄ electrolytes [140]. However, when the electrolyte was replaced by H₂SO₄, Pt(100) was found to be more active than Pt(111) [141–143]. This activity difference was attributed to the special adsorption behaviors of the bisulfate anion on Pt(111). The bisulfate anions can be adsorbed on the Pt(111) surface more strongly than on Pt(100), resulting in an impeditive ORR process. Systematic investigations confirmed that the different properties of the respective facets have a significant effect on their catalytic performance. Following this work, many studies focused on developing a facet-control method to construct more active facets on a catalytic surface, from ideal single-crystal metals to more practical

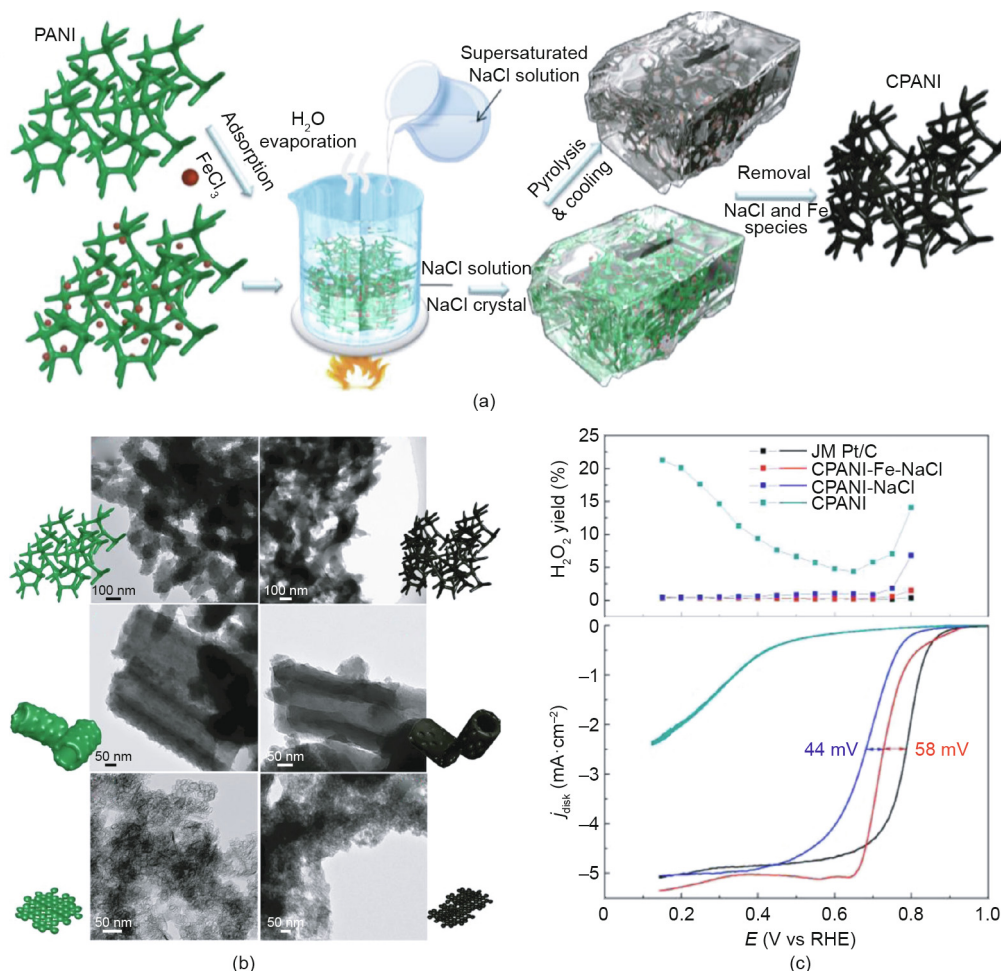


Fig. 6. (a) Schematics of the salt recrystallization method for shape fixing; (b) transmission electron microscope (TEM) images of synthesized 3D PANI and their corresponding carbonized products (CPANI); (c) H₂O₂ yield curves and ORR curves of different samples. JM: Johnson Matthey. Reproduced from Ref. [119] with permission of ACS Publications, ©2015.

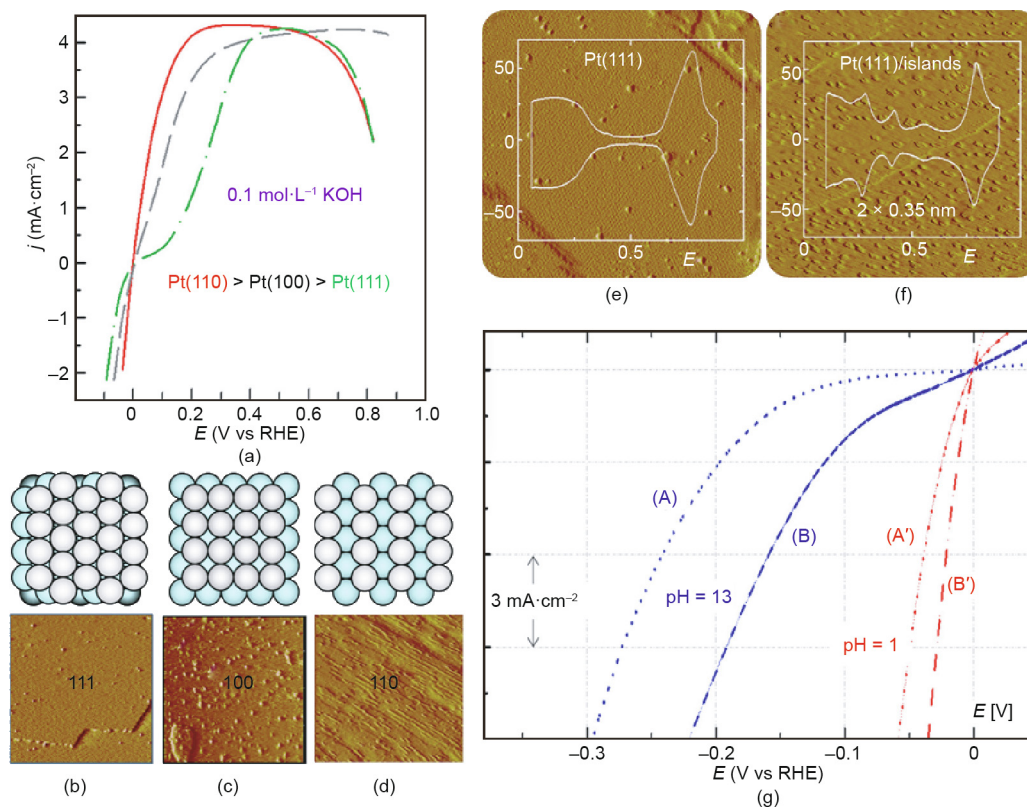


Fig. 7. (a) HER/HOR on different facet surfaces of Pt; (b–d) STM images of different facets of Pt (the insets are their corresponding structural models STM images for (e) the prepared Pt(111) and (f) the Pt islands/Pt(111) surface; (g) the HER electrochemical responses of the two Pt facets. (a–d) reproduced from Ref. [126] with permission of ACS Publications, ©2008; (e, f) reproduced from Ref. [130] with permission of Springer Nature Limited, ©2013.

nanomaterials [144–150]. Narayanan and El-Sayed [144] were the first to demonstrate facet-controlled synthesis in the case of Pt nanocrystals, including (100)-terminated nanocubes, (111)-bounded nanotetrahedra, and nanospheres with both (111) and (100) facets. A high-temperature organic phase method was reported by Wang et al. [145] for the synthesis of monodispersed (100)-terminated Pt nanocubes for ORR. The facet-controlled Pt nanocubes showed a specific ORR activity that was more than double the activity of a commercial Pt catalyst in acid electrolyte.

Because of the higher density of low-coordinated atoms, steps, edges, and kinks, metals and compounds with high-index facets generally possess greatly improved reactivity in comparison with typical low-index materials [151]. However, such high-index facets are thermodynamically unstable due to their higher surface energy [152,153]. Accordingly, the synthesis of high-index faceted nanomaterials has become a herculean task. In the last few years, a wide variety of synthetic protocols have been exploited for the synthesis of metallic nanomaterials with high-index facets for the purpose of improved catalytic reactivity. Yu et al. [154] developed a simple reduction route in aqueous solution to prepare Pt concave nanocubes (c-NCs) enclosed by high-index facets of (510), (720), and (830). Pt c-NCs have also been fabricated by using glycine to manipulate the reduction kinetics of H₂PtCl₆ [155]. Employing electrochemical means, Tian et al. [156] synthesized tetrahedral (THH) Pt nanocrystals with facets including (730), (210), and (520). In addition to these single-metal materials, multi-metallic high-index faceted nanocrystals have been developed [157–160]. As shown in Fig. 8, Luo et al. [159] reported a new class of Pt₃Fe zigzag-like nanowires (z-NWs) with stable high-index facets and a nanosegregated Pt-skin structure. These unique structural features endowed the Pt-skin Pt₃Fe z-NWs with a mass and specific

ORR activity of 2.11 A·mg⁻¹ and 4.34 mA·cm⁻², respectively, at 0.9 V vs RHE.

With the purpose of reducing catalyst cost, the design and preparation of low-cost metal nanomaterials with different exposed reactive facets have been a recent trend in facet engineering [161–167]. Su et al. [168] studied the growth mechanism of the NiO crystal and found that the surface energy of the NiO facets followed the order of (100) < (113) < (101) ≈ (110). Han et al. [161] provided a template-free hydrothermal method for the controllable fabrication of a surface-tailored Co₃O₄ nanocube (NC), nano-truncated octahedron (NTO), and nanopolyhedron (NP), with facets of (001), (112), (001) and (111). The different crystal planes endowed the Co₃O₄ nanocrystal with different exposed surface atomic configurations of the Co²⁺ and Co³⁺ active sites. The unusual (112) plane-enclosed Co₃O₄ nanoparticle on reduced graphene oxide (rGO) with abundant Co³⁺ sites exhibited superior activity for both OER and ORR. In addition to these metal oxides, many other metal compounds with special facets have been reported. Feng et al. [163] further synthesized Ni₃S₂ nanosheet arrays with stable (210) facets, and demonstrated them to be efficient and ultra-stable electrocatalysts for HER and OER. Wang et al. [162] obtained flower-like nickel phosphide with different crystalline structures (Ni₅P₄ and Ni₂P) and ascribed the excellent HER activity to the hierarchical structure with high-energy (001) facets.

3.3. Polymorph engineering

Apart from tuning the exposed facets of the nanocrystal, modulating the atomic scale arrangement (i.e., the transformation of the crystalline phase) can affect the intrinsic activity of a catalyst, due

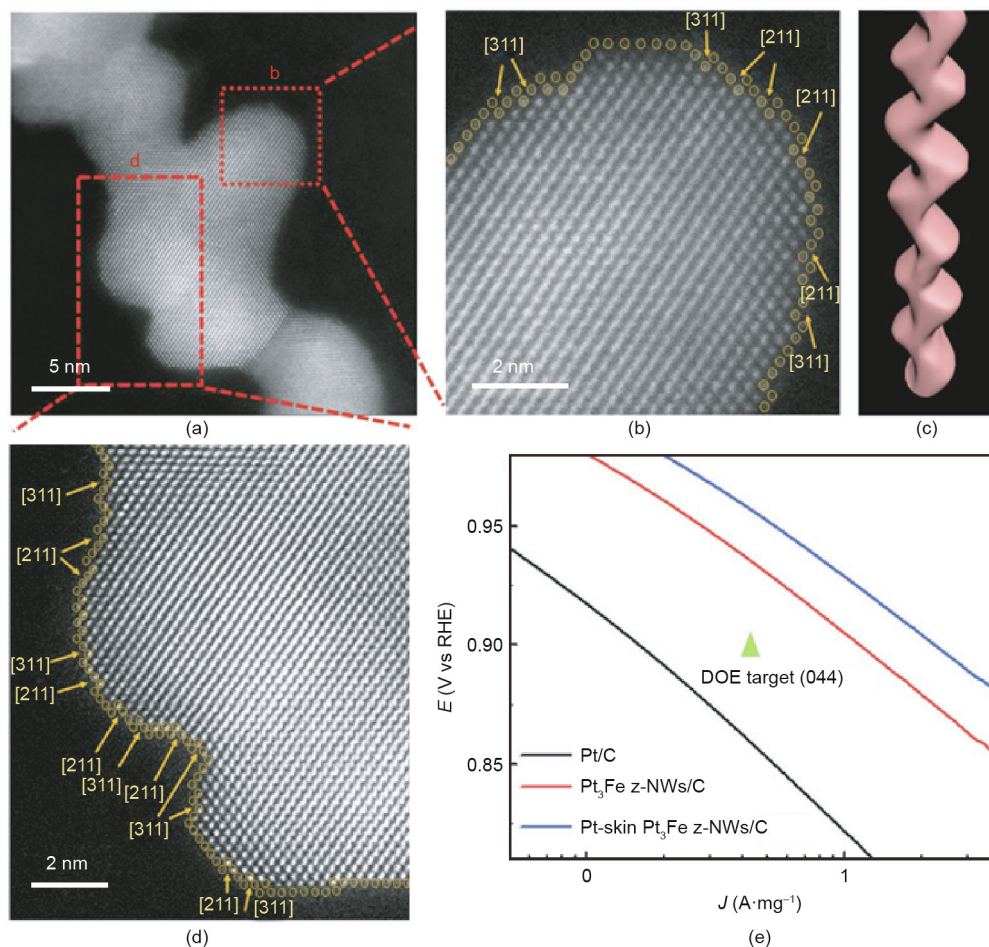


Fig. 8. (a) High-angle annular dark field (HAADF)-TEM image of Pt-skin Pt₃Fe z-NWs; (b, d) enlarged images of the red square in (a); (c) structural demonstration of the z-NWs; (e) ORR mass activity Tafel plots for commercial Pt/C, Pt₃Fe z-NWs/C, and Pt-skin Pt₃Fe z-NWs/C. DOE: department of Energy. Reproduced from Ref. [159] with permission of WILEY-VCH Verlag GmbH & Co. KGaA, ©2018.

to the fundamental changes in its physical and chemical properties. Transition-metal disulfides with several unique polymorphs are typical cases that have been widely studied. Among these polymorphs, the metastable 1T phase has recently aroused great research interest owing to its metallic behavior, which is beneficial to electrocatalytic processes [169–174]. Lukowski et al. [169] synthesized metallic 1T-MoS₂ nanosheets from semiconducting 2H-MoS₂ via a lithium intercalation method. The resulting 1T-MoS₂ exhibited a dramatic improvement in electrocatalytic HER performance compared with the corresponding 2H polymorphs (Fig. 9). Similarly, metallic 1T tungsten disulfide (1T-Ws₂) was further synthesized by Lukowski et al. [173] via a simpler microwave-assisted intercalation. The polymorph engineering endowed the 1T-Ws₂ with faster electrical conductivity and more intensive active sites, boosting its HER activity.

Not only can unique properties be induced by atomic arrangement, but the active sites of 1T-catalysts may also differ from those of the traditional 2H-structured phase. In this context, Voiry et al. [175] obtained highly conductive 1T-MoS₂ nanosheets with excellent HER activity after removing excess negative charges from the surface of chemically exfoliated MoS₂ nanosheets. Interestingly, after partial oxidation of the 1T- and 2H-MoS₂, a sharp contrast in HER activity changes was observed. Although there was almost no shift in the HER activity of 1T-MoS₂ after edge oxidation, the activity of 2H-MoS₂ seriously decreased. It is well known that the edges of the usual 2H-MoS₂ crystal are the main active sites for HER. The significant difference in HER activity between the par-

tially oxidized 1T- and 2H-MoS₂ nanosheets revealed that the main active sites of 1T-MoS₂ for driving HER catalysis are not the edges of the nanosheets, but the basal planes of the nanosheets.

The catalytic performance of metal oxides may also vary with their crystal phases. Our group found that reversing spinel crystalline structure has a great influence on the ORR catalytic activity of spinel (Fig. 10) [176,177]. By adjusting the iron (Fe) content, the spinel structure of a Co-Fe-based crystal can be changed from its normal structure to the inverse structure and then back again [178]. The electrochemical results revealed that the inverse spinel {Co}[FeCo]O₄/NG (nitrogen doped graphene) had the best ORR activity, outperforming commercial Pt/C. DFT results further disclosed that the higher ORR activity of the inverse-structured {Co}[FeCo]O₄ could be ascribed to the modulated oxygen adsorption energy and elongated adsorbed oxygen bond induced by the dissimilarity effect of Fe and Co atoms at the octahedral site. The effect of crystal phase on the reaction pathway of ORR has also been studied. Karunakaran et al. [179] synthesized four kinds of iron oxide nanoparticles with different phases incorporated inside 3D rGO aerogels and determined their electrochemical, catalytic, and electron transfer properties for ORR. The results showed that ORR was catalyzed by all four catalysts via a two-electron pathway under higher potentials (0.70 V). On the other hand, when the potentials decrease to 0.20 V, rGO composites containing magnetite, maghemite, and goethite proceeded via four-electron transfer kinetics, whereas the hematite-containing composite went through two-electron transfer kinetics.

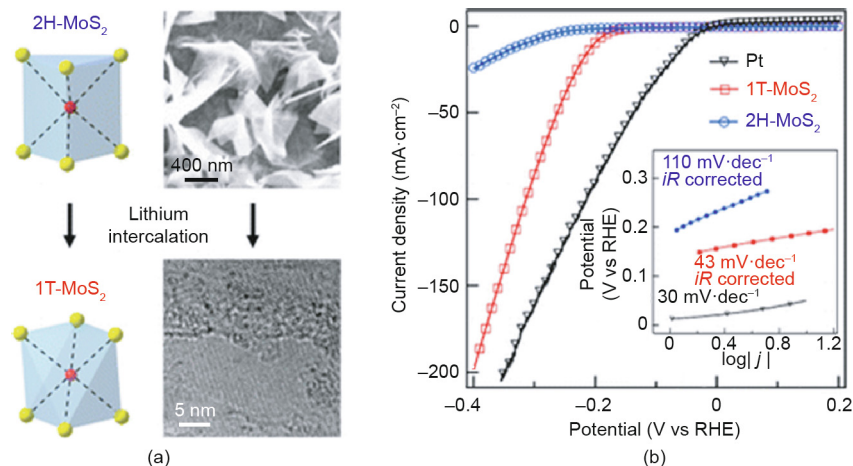


Fig. 9. (a) Phase transition of semiconducting 2H-MX₂ to metallic 1T-MX₂ via lithium intercalation; (b) HER polarization curves for both forms of MoS₂. Reproduced from Ref. [169] with permission of ACS Publications, ©2013.

Configuration distortion induced by the Jahn–Teller effect for transition-metal compounds has also been studied in relation to the electrocatalytic performances of such compounds [180]. Recently, Liu et al. [181] observed an obvious structural distortion in Co₃S₄ atomically thin nanosheets (CSATNs) via the ultrasound exfoliation treatment of an intermediate Co₃S₄/TETA hybrid precursor. The structural distortion of CSATNs generates an electronic configuration change. Compared with bulk samples, the shift from spectral to lower magnetic fields (Figs. 11(a) and (b)) implies that the spin state of Co³⁺ in the octahedral sites ($t_{2g}^4e_g^2$) of CSATNs adjusts from low spin to high spin. High-angle annular dark field (HAADF) images showed that the octahedral coordinated cations were solely exposed in the planes, which further revealed the existence of Jahn–Teller elongation (Figs. 11(c)–(f)). Due to the synergistic adjustment in the atom and electron configuration, CSATNs possess significantly enhanced OER performance in comparison with bulk samples. In fact, the Jahn–Teller effect is attributed to the uneven electron distribution of the central ions in degenerate d orbitals (t_{2g} or e_g). Thus, the filling state of electrons in the e_g orbital may have a significant role in the catalytic properties of the transition-metal compounds. A volcano relationship between the intrinsic ORR activity and the filling states of the e_g orbital in the B ions of perovskite-based oxides (ABO₃) was discovered by Suntivich et al. (Fig. 11(g)) [182]. The perovskite-based oxides with

only one electron filling in the e_g orbital (defined as $e_g \approx 1$) were demonstrated to possess the highest ORR activity, as O₂ can adsorb on the B sites end-on with an optimal binding energy. The e_g occupancy theory can be further extended to spinel oxides, although the ORR active sites of spinel are not tetrahedral sites but octahedral sites (Fig. 11(h)) [183].

3.4. Amorphization

Amorphization to modulate the atomic scale arrangement, and thus increase the catalytic performance, is another research hotspot [184–189]. Short-range atomic arrangements of amorphous phases are beneficial for increasing the density of active sites [190–194]. As early as 1995, Weber et al. [190] investigated the structural units of the amorphous compound MoS₃ and found that all molybdenum is present in the Mo⁴⁺ oxidation state, while sulfur atoms occur in two different types of coordination: S²⁻ and S²⁻. Merki et al. [191] and Benck et al. [192] then confirmed that the amorphous MoS₂ is more active in catalyzing HER. Structural measurements demonstrated that an amorphous MoS_x film is extremely rough in surface and sulfur-rich in composition, resulting in a large active area and intensive active sites for HER catalysis. Benck et al. [192] further revealed that the increase in the HER activity of amorphous molybdenum sulfide is contributed to by

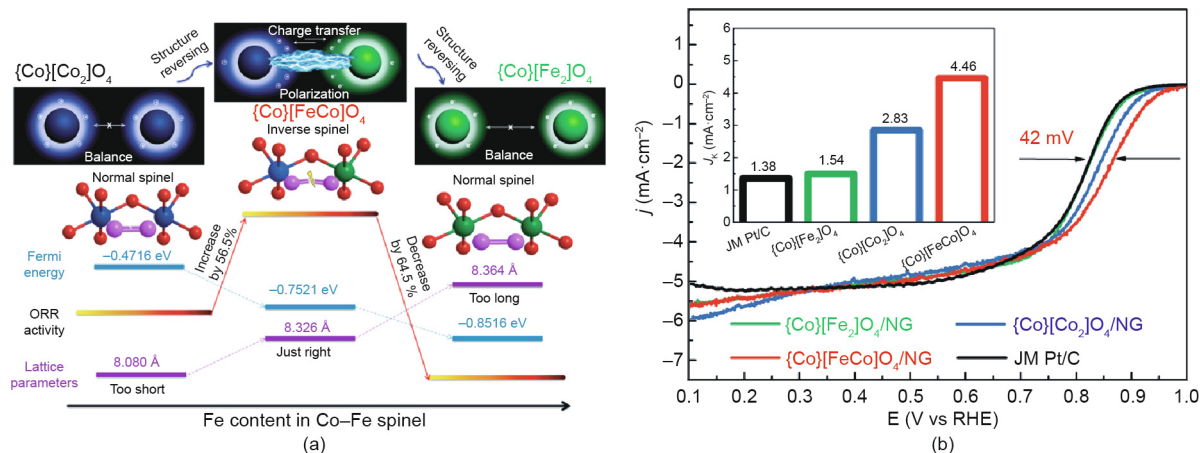


Fig. 10. (a) Structure reversing and the relationships between ORR properties; (b) the ORR activities of {Co}[Fe₂]O₄/NG, {Co}[Co₂]O₄/NG, {Co}[FeCo]O₄/NG, and Pt/C. Reproduced from Ref. [176] with permission of WILEY-VCH Verlag GmbH & Co. KGaA, ©2016.

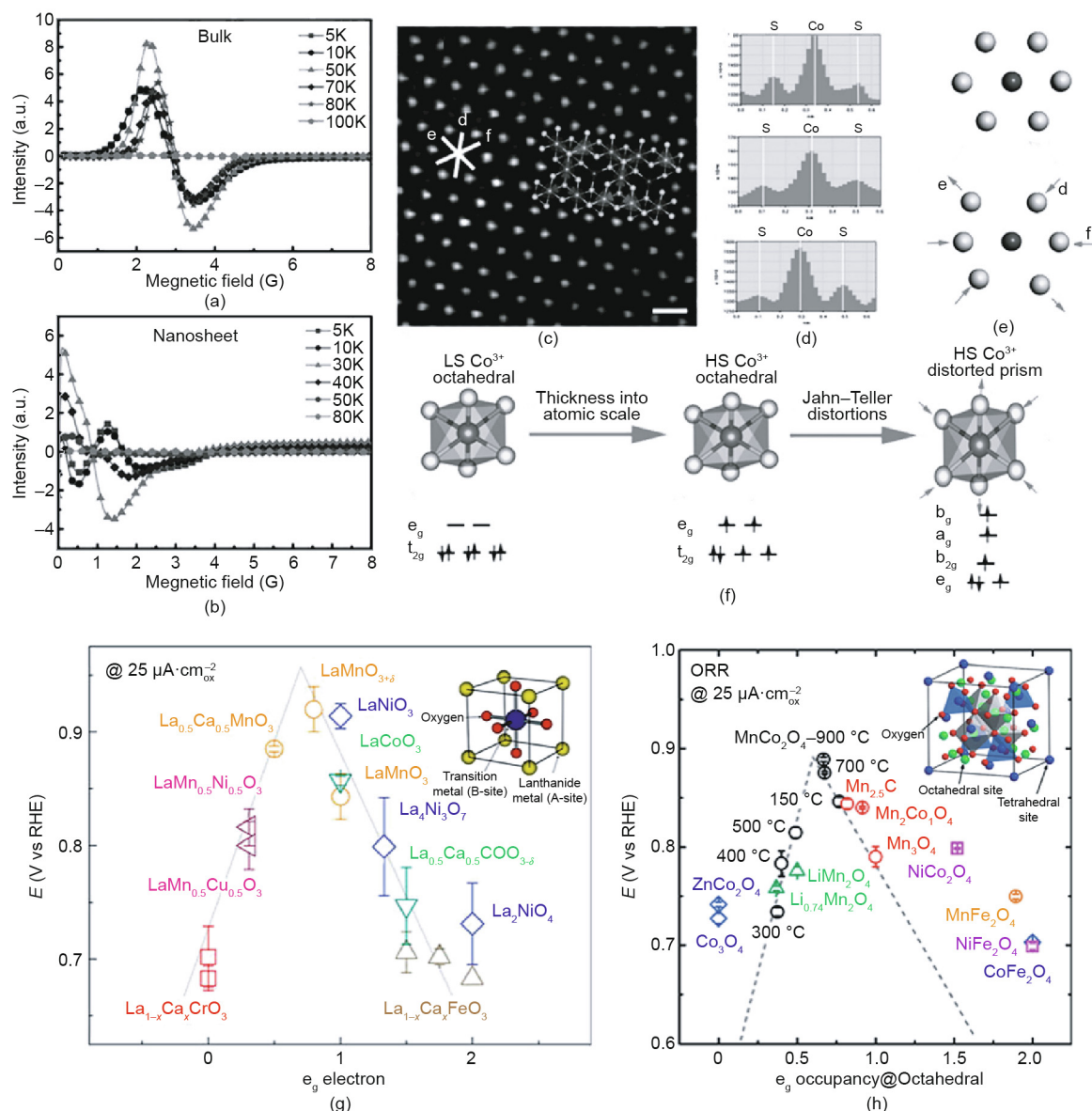


Fig. 11. (a, b) Electron paramagnetic resonance (EPR) of bulk and CSATNs; (c) HAADF image and (d) intensity line profiles of CSATNs; (e) schematic of the Jahn-Teller distortion and (f) structural transformation; (g) ORR activities of perovskite oxides as a function of the e_g electrons; (h) role of e_g occupancy of the active element at the octahedral site in the ORR activities of spinel oxides. (a–f) reproduced from Ref. [181] with permission of WILEY-VCH Verlag GmbH & Co. KGaA, ©2015; (g, h) reproduced from Ref. [183] with permission of WILEY-VCH Verlag GmbH & Co. KGaA, ©2017.

the large number of active sites caused by the amorphous structure and rough, nanostructured morphology, as the activity scales with the electrochemically active surface area. Meanwhile, Li et al. [195] and Li et al. [196] systematically studied the origin of the catalytic activity of the amorphous MoS_2 in terms of the composition and crystallinity. Interestingly, the experimental results revealed that the crystallinity is crucial for determining the catalytic performance, whereas the composition is not particularly significant.

In addition to the HER catalysis, Smith et al. [185] demonstrated that amorphous materials are more active than the comparable crystalline materials for OER catalysis, based on a study of the mixed-metal oxides of iron, nickel (Ni), and cobalt (Co). Due to the amorphous structure, the distribution of the metals in the amorphous films is homogeneous and their compositions can be accurately controlled. Modulated $a\text{-Fe}_{100-y-z}\text{Co}_y\text{Ni}_z\text{O}_x$ with an optimal element content exhibited excellent catalytic property that was even comparable to that of commercial noble metal oxide catalysts. Thanks to the controllable composition of amorphous

materials, the effect of metal composition on electrocatalytic performance can be further studied along with the effect of amorphization. Smith et al. [184] prepared 21 complex metal oxide films for electrocatalytic water oxidation, and demonstrated the excellent stoichiometric concentrations of Fe, Co, and Ni in each sample. Structural characterization and electrochemical measurement confirmed that iron content is important for lowering the Tafel slope, and that cobalt or nickel are beneficial in reducing the overpotential (Fig. 12). For scale-up production, Kuai et al. [186] proposed an aerosol-spray-assisted method by which amorphous mixed-metal oxides can be sustainably obtained, which is very suitable for industrial applications. The obtained $\text{Fe}_6\text{Ni}_{10}\text{O}_x$ exhibited a low overpotential of 0.286 V for driving $10 \text{ mA}\cdot\text{cm}^{-2}$ and a small Tafel slope of $48 \text{ mV}\cdot\text{decade}^{-1}$ for the electrochemical OER, exceeding the best catalytic performance of all investigated Fe–Ni–O_x series.

Although the active sites of amorphous catalysts can be greatly enhanced by amorphous engineering, the electrical conductivity of

the amorphous materials will be decreased due to short-range disorder in the crystal structure. Coupling these low-conductive materials with highly conductive materials is an effective route to guarantee the excellent electrocatalytic performance of amorphous catalysts. For example, Lee et al. [197] synthesized amorphous MnO_x nanowires supported by Ketjenblack (KB) carbon as highly efficient ORR electrodes. The low-cost and highly conductive KB acts as a supporting matrix for the catalyst, greatly accelerating the electron transfer during the electrocatalytic processes. Many other amorphous/conductive composite materials, such as amorphous MoS_x /carbon composite catalyst [198], amorphous MoS_x /polypyrrole copolymer film (PPy/ MoS_x) [199], and amorphous MoS_x /N-doped CNT (NCNT) forest hybrid catalyst [200], have also been reported. The highly conductive skeletons in these composite materials can overcome the barriers induced by the low electrical conductivity of amorphous catalysts, leading to a remarkable increase in catalytic activity (Fig. 13). Porous metal nanostructures, such as Ni foam [201] and nanoporous gold [202], are also used as conductive substrates to support an amorphous MoS_x catalyst, of which the HER activity can be significantly enhanced.

3.5. Defect engineering

Defects exist widely in nanomaterials. It has been realized that the surface of catalysts with defects always exhibit higher reactivity than the defect-free sites [203–206]. Accordingly, defect engineering has gradually developed as an effective method to tune the electronic and surface properties of nanomaterials [207–209]. Cheng et al. [210] synthesized tetragonal or cubic $\text{M}_x\text{Mn}_{3-x}\text{O}_4$ spinels by reducing the amorphous MnO_2 in aqueous M^{2+} solution under ambient conditions. Due to its highly active area and abundant defects, nanocrystalline $\text{Co}_x\text{Mn}_{3-x}\text{O}_4$ is endowed with considerable catalytic activity for both ORR and OER. Similarly, Ma et al. [211] synthesized oxygen vacancy (OV) defect-rich mesoporous MnCo_2O_4 materials, and found that their stability and methanol tolerance ability even exceeded those of a Pt/C catalyst. In order to obtain insight into the effect of defects in catalytic performance, our group performed a DFT + U calculation of OV concentration on the electronic structure of $\beta\text{-MnO}_2$ catalysts and their catalytic performance for ORR [212]. As shown in Fig. 14, a moderate concentration of bulk OVs will greatly increase the electric conductivity of MnO_2 , while excessive OVs will hinder the ORR process. Such a curvilinear relationship between the electronic structure and OV concentration suggests that the conductivity and ORR catalytic activity of $\beta\text{-MnO}_2$ can be modulated by the OV concentration. Defect engineering can also be applied to increase the density of

active sites of nanomaterials for electrocatalysis [203,213,214]. Xie et al. [203] designed a reaction with a high concentration of thiourea, thus realizing controllable defect modulation in as-formed MoS_2 ultrathin nanosheets. Due to the defect-rich structure, many tiny cracks formed on the basal surfaces, resulting in 13 times more active sites for the defect-rich MoS_2 ultrathin nanosheets than for the defect-free MoS_2 .

Similar to element vacancy in metal compounds, intrinsic defects in carbon-based electrocatalysts are universal but have been ignored for a long time [209]. Defects easily form after heteroatom doping, and act as the active sites favoring electrocatalysis [215,216]. However, the electrocatalytic reactivity of carbon-based materials has mainly been ascribed to the induced changes of heteroatoms doping. As time goes on, some research has found that the catalytic activity of carbon electrocatalysts with intrinsic defects is even better than that of heteroatoms-doped carbon materials [217,218]. For example, Jiang et al. [219] found that defective carbon nanocages (CNC) possess a high ORR activity that exceeds that of B-doped carbon nanotubes. In this case, defect-rich CNC were successfully synthesized with many typical defect locations, but without any dopants (Fig. 15(a)). The electrochemical results indicated that the resultant CNC material with the highest defect density showed the best electrochemical ORR activity (Fig. 15(c)). The DFT results further indicated that the high ORR activities of these defect materials could be attributed to the pentagon and zigzag edge defects (Fig. 15(d)). Zhao et al. [220] used first principles calculations to predict that a type of 585 defect on graphene would be even more active than the N-doped sites for ORR, and obtained strong support for this theoretical prediction through experimental investigations. With the defect mechanism in mind, Zhao et al. [221] prepared a porous carbon (PC) material lacking any elemental doping by carbonizing Zn-MOF at 950 °C. With the benefit of the removal of zinc (Zn) atoms, defects could be formed on the PC catalyst, endowing the PC catalyst not only with excellent ORR activity, but also with a stability comparable to that of a commercial Pt/C catalyst. Furthermore, with the exception of the ORR process, the individual electrocatalytic activities for the other three electrochemical reactions in the energy conversion from water—that is, HOR, OER, and HER—were demonstrated to be particularly sensitive to the types of defects derived by the removal of heteroatoms from graphene [222].

3.6. Atomic doping

Atomic doping is the most widely used strategy for modulating the properties of catalytic materials. By reasonably introducing one

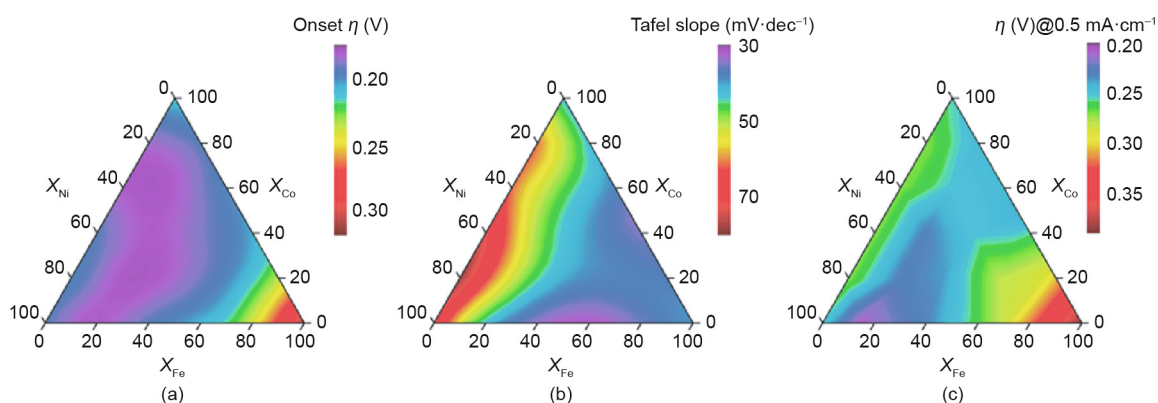


Fig. 12. Contour plots for the activity parameters of amorphous metal oxide films with different metal contents. (a) Onset potential; (b) Tafel slopes; (c) overpotential at $j = 0.5 \text{ mA}\cdot\text{cm}^{-2}$. Reproduced from Ref. [184] with permission of ACS Publications, ©2013.

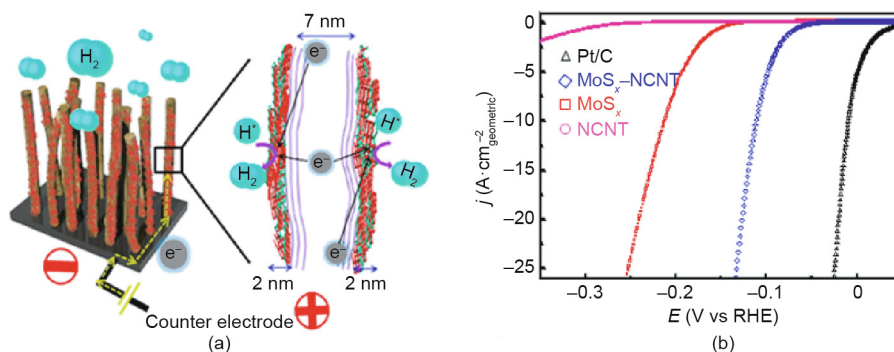


Fig. 13. Electrochemical catalytic activities. (a) HER scheme for MoS_x/NCNT forest hybrid catalyst; (b) HER activities of different samples. Reproduced from Ref. [200] with permission of ACS Publications, ©2014.

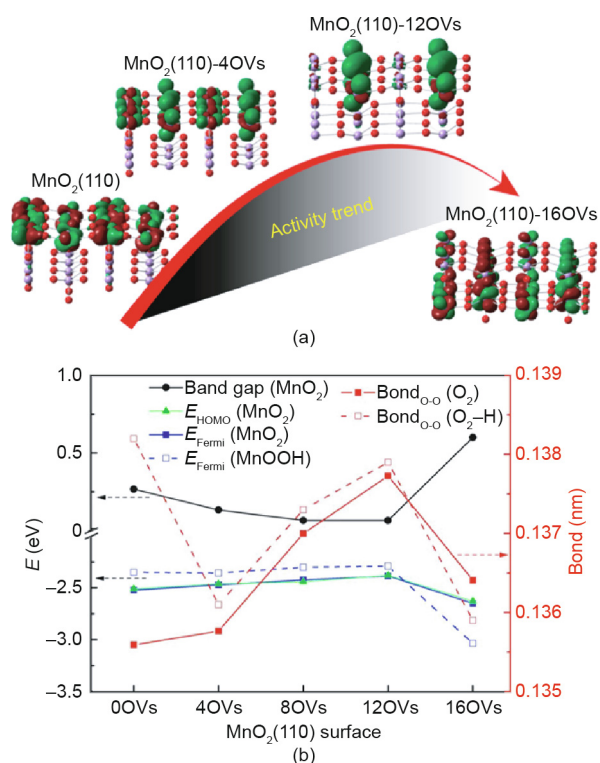


Fig. 14. (a) Activity trend of MnO_2 with different OV concentrations; (b) changes of DFT results as a function of OV concentration. HOMO: highest occupied molecular orbital. Reproduced from Ref. [212] with permission of ACS Publications, ©2015.

or more metallic or nonmetallic elements into the lattice of the material, the electron structure of the original material can be adjusted, thus effectively improving the catalytic performance of the material [223–232]. Taking MoS_2 as an example, many metallic elements such as Ni, Co, Fe, vanadium (V), lithium (Li), and copper (Cu) have been reported to be successfully doped into its crystal structure, positively affecting the physical and chemical properties [171,233–237]. Among these doped metallic elements, Ni and Co tend to locate around the S in MoS_2 , which will decrease the hydrogen adsorption energy at the S edge and increase the density of the active sites in MoS_2 [233–235]. Unlike Ni- and Co-doped MoS_2 , V doping cannot increase the number of active sites, but will enhance the conductivity of MoS_2 [236]. Interestingly, our group explored the influence of the Ni-doping of molybdenum carbide on its surface electronic structure and its relationship with HER performance by combining experimental and theoretical evidence [97].

As shown in Figs. 16(a)–(d), one-dimensional (1D) NiMo_2C nanowire arrays were directly constructed onto conductive 3D Ni foam ($\text{NiMo}_2\text{C}/\text{NF}$) via a facile and controllable strategy combined with hydrothermal and post-carburization treatment. The binder-free integrated $\text{NiMo}_2\text{C}/\text{NF}$ electrode showed superb HER catalytic activity in comparison with Mo_2C and Ni catalysts (Fig. 16(e)). The DFT calculations clearly demonstrated that the incorporation of Ni into the Mo_2C lattice brought about changes in the charge distribution on the catalyst, which resulted in a synergistic effect of Ni and Mo_2C that decreased the hydrogen binding energy (Figs. 16(f) and (g)).

Apart from metallic elements, research on doping with non-metallic elements is also very active. Xie et al. [238] successfully synthesized oxygen-doped MoS_2 ultrathin nanosheets, on which the synergistic modulations of both the active sites and the conductivity could be rationally realized. According to the DFT calculations, the smaller differential binding free energy of the oxygen-incorporated MoS_2 revealed a lower energy barrier for driving the HER process. Our group further proposed a partial phosphorization of metal oxide precursors to construct oxygen-incorporated NiMoP_2 with enhanced HER activity [239]. As illustrated in Figs. 16(h)–(i), the H adsorption energy on the NiMoP_2 surface was optimized by the oxygen incorporation, as the ΔG_{H^*} of the O- NiMoP_2 is much closer to zero than its undoped equivalent. In addition, the Ni and Mo in O- NiMoP_2 possessed more positive charge, which was beneficial for adsorbing and activating water molecules, greatly accelerating the water dissociation in the alkaline HER.

Aside from these metal compounds, carbon-based materials have been intensively used as doping objects, greatly enlarging the scope of catalyst research [240–245]. Early in 2013, our group reported a phosphorus (P)-doped graphene with an ORR catalytic performance comparable to that of commercial Pt/C [246]. Furthermore, N, P dual-doped graphene/carbon materials were prepared as electrocatalysts for both ORR and OER, and their catalytic activities exceeded those of the benchmark Pt/C catalyst [247]. In order to reveal the underlying reasons for the high activity of the heteroatom-doped carbon, our group conducted a comprehensive DFT calculation on graphene doped by a series of different heteroatoms for ORR [248]. The DFT results indicated that there was a triple effect of the carbon sites—namely, the charge, spin density, and ligand effect—determining the intrinsic catalytic activity of the doped carbon catalysts and their ORR mechanism (Fig. 17). When the carbon materials are doped by a single heteroatom, the carbon sites around the doped atom can only be activated by the triple effect separately. This causes the ORR to proceed via the associative mechanism, and there is a limitation with an intrinsic overpotential of 0.44 V. However, when carbon materials are doped by metal or dual-heteroatoms, the ORR follows the dissociative mechanism,

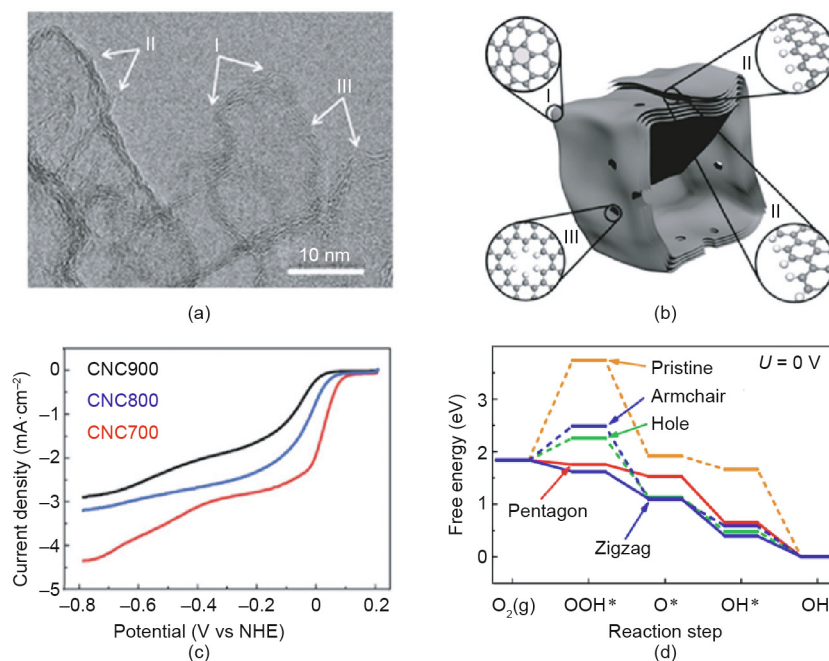


Fig. 15. (a) HRTEM (high resolution TEM) image and (b) schematic structure of CNC700; (c) rotating disk electrode (RDE) curves of these CNC samples; (d) ORR free-energy diagrams of different defects. Reproduced from Ref. [219] with permission of ACS Publications, ©2015.

as double carbon sites can be activated by the triple effect. Thus, the activity limitation of the associative mechanism will no longer be in effect, leading to enhanced ORR activity. Our group also synthesized graphene co-doped with metallic and nonmetallic elements, and revealed the roles of nitrogen configuration in N-doped graphene as well as that of the trace atomic Ni in HER [249]. We found that quaternary nitrogen (N) is the most active site of the three N types in HER, whereas when doping with trace atomic cobalt, the planar (pyridine and pyrrolic) N becomes the most active. In contrast, when trace atomic Co was replaced by Ni, the planar (pyridine and pyrrolic) N exhibited depressed HER activity.

3.7. Interface engineering

Hybrid nanomaterials have an interface located at the boundary of two components [250]. It is extremely important for a heterogeneous catalyst to have a proper interfacial structure because the interface region always presents unique physical and chemical properties [251]. These unique properties can facilitate the capability of the resultant material to bind, convert, and transport the surface species (e.g., adsorbents, electrons, and intermediates), greatly promoting the catalytic reactions occurring on the surface [252–255]. In recent years, abundant research studies have reported the design and synthesis of electrocatalysts for water–hydrogen electroconversion with the assistance of interface engineering. In general, depending on the relative locations of the components, hybrid materials can be classified as supported structures, heterostructures, or core–shell structures [256]. The special character of a supported structure is that the support component is much larger than the other components; in contrast, the components in a heterostructured material have similar sizes. In a core–shell structure, one component is covered by another component, with interfaces existing at the boundary between the two components. These three types of hybrid materials with different interface structures have been reported as a result of research assembling metals, metal oxides, nonoxides, and so forth. For

example, Zhang et al. [257] reported on a MoNi_4 electrocatalyst immobilized on MoO_2 cuboids ($\text{MoNi}_4/\text{MoO}_2@Ni$) with a supported structure that was made by controlling the outward diffusion of nickel atoms during calcination. By heating the NiMoO_4 precursor under a reduction atmosphere, MoNi_4 nanoparticles (20–100 nm) supported by MoO_2 cuboids ($\sim 1 \mu\text{m}$) were synthesized, and the supported hybrid catalyst was found to exhibit excellent HER activity in alkaline solution (Figs. 18(a) and (b)). Heterostructured Co/CoP nanoparticles were prepared by Xue et al. [258] via the gradual phosphidation of Co metal into CoP components. By changing the weight ratios of the NaH_2PO_2 and Co species, the CoP contents in Janus Co/CoP nanoparticles could be controllably modulated, affecting the interface zone in the Co/CoP catalyst (Figs. 18(c)–(f)). As illustrated in Figs. 18(g) and (h), Xu et al. [259] fabricated NiCo-based porous microrod arrays composed of carbon-confined NiCo@NiCoO₂/C core@shell nanoparticles (NiCo@NiCoO₂/C PMRAs (porous microrod arrays)) by the reductive carbonization of bimetallic (Ni, Co) metal–organic framework microrod arrays and subsequent controlled oxidative calcination. The obtained NiCo@NiCoO₂/C PMRAs combined several desirable qualities for OER, including a large surface area, good conductivity, and multiple electrocatalytic active sites.

For the purpose of rational catalyst design, the origin of the enhanced catalytic performance of these hybrid materials with an abundant interface has been deeply explored. The modulation of the electronic structure in the interface of hybrid materials has been well proven [260–267]. An observed electron transfer was evidenced by Yu et al. [268] using X-ray absorption near-edge spectroscopy (XANES) for a Ni(OH)₂/Pt catalyst. As pointed out by the authors, the pre-edge and main absorption edge of Ni for both the α - and β -Ni(OH)₂/Pt electrode are shifted to lower energies, and the absorption intensities decrease in comparison with their counterparts, demonstrating that the electrons transfer from the Pt substrate to the hydroxide. Han et al. [269] revealed a strong metal–support interaction (SMSI) effect between CoS₂ and Pt in the Pt/CoS₂ hybrid system for highly active water splitting. A downward shift in the Pt d-band structure was proved by DFT

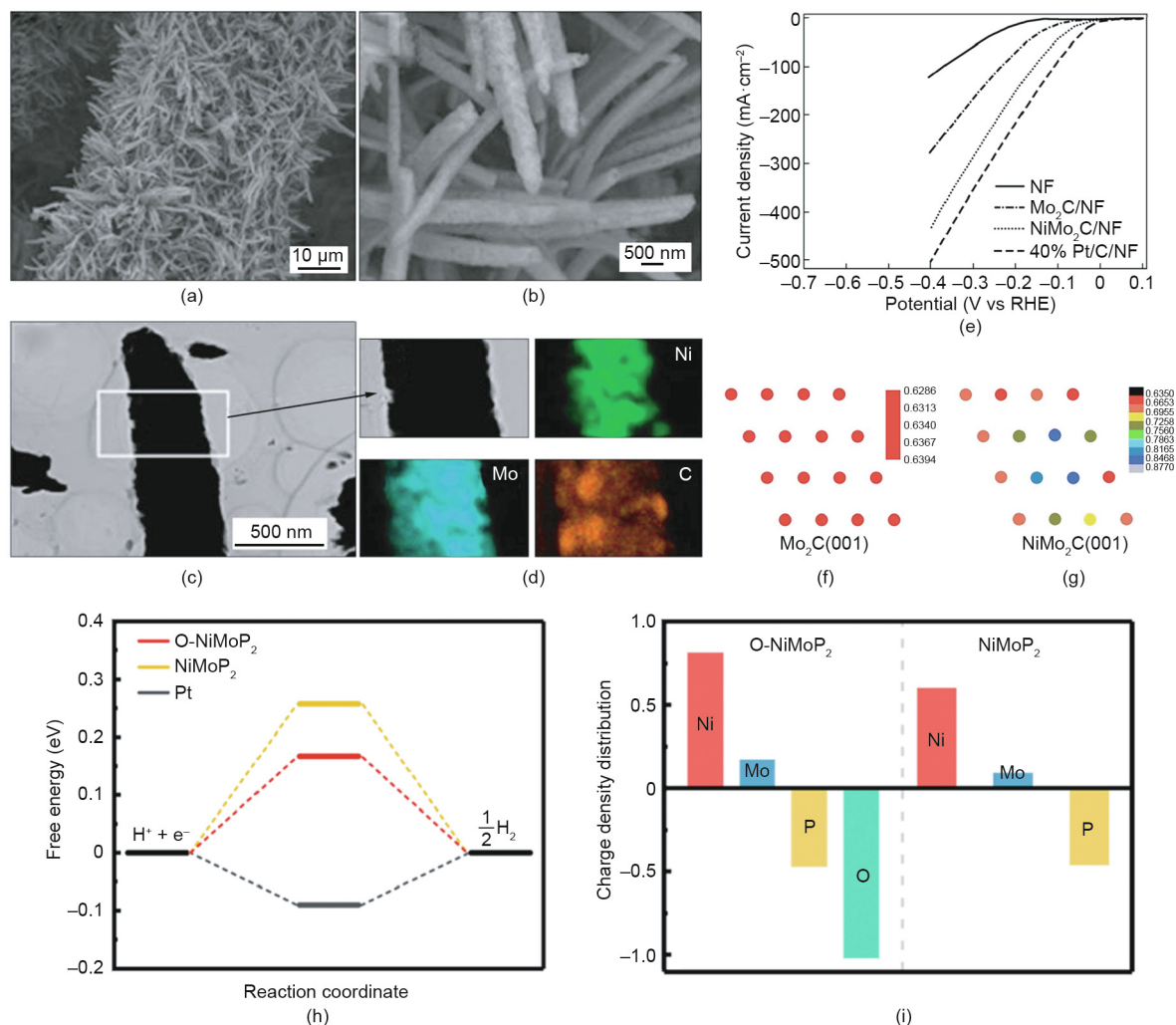


Fig. 16. (a–d) SEM, TEM, and EDX (energy dispersive X-ray spectroscopy) images and (e) electrochemical characterization of NiMo₂C electrodes; distribution of Bader charge of (f) Mo₂C(001) and (g) NiMo₂C(001); (h) hydrogen free-energy and (i) charge density distributions on different samples. (a–g) reproduced from Ref. [97] with permission of Royal Society of Chemistry, ©2015; (h, i) reproduced from Ref. [239] with permission of ACS Publications, ©2018.

calculation and was further supported by X-ray photoelectron spectroscopy (XPS) and X-ray absorption fine structure (XAFS) analyses. Although the electron transfer has been well demonstrated in these metal/metal compound catalysts, the underlying mechanisms for the high catalytic activity are ambiguous. In order to uncover this mystery, our group studied the chemical properties of the metal/metal oxide interface, and found an interface-induced synergistic effect—the “chimney effect” (Figs. 19(a) and (b)) [270]. As revealed by the DFT results (Figs. 19(c) and (d)), the neighboring sites around the interface are immune to H₂O* and OH* species but selectively adsorb H*, which prevents the poison effect of H₂O* and OH* on active sites. Meanwhile, the active sites on the interface have good capability for the adsorption and desorption of the H* reactant for the H₂ product, as its ΔG_{H^*} is close to 0. Due to these features, the hydrogen evolution on metal oxide/metal catalysts behaves similarly to a chimney for generating hydrogen product continuously. The strong positive correlation between the HER activity of the metal oxide/metal composites and the interfacial metal atoms (Fig. 19(e)) further confirmed that the hydrogen generation can be greatly accelerated by increasing the amount of active site. With the exception of metal/metal compound catalysts, the origin of the performance enhancement of metal compound hybrid catalysts was further investigated by our group through the casting of monometallic NiO–Ni₃S₂ heteronanoshells [271].

The electron transfer from Ni–S to Ni–O that occurs at the interface of NiO–Ni₃S₂ results in a superior activity of overall water splitting that is even superior to the benchmark Pt/C and RuO₂ assembly (Fig. 19(g)). DFT calculation results further demonstrated that the activation barrier of the hydrogen (or oxygen-containing) intermediates on the NiO–Ni₃S₂ interfaces are significantly lowered, which is beneficial for the OER and HER processes (Figs. 19 (h) and (i)).

Vacancy generation is another important factor in developing interfaced materials with improved catalytic performances [272–277]. A typical example was reported by Li et al. [278], who prepared FeS₂/CoS₂ hybrid nanosheets (NSs) for overall water electrolysis. In the synthesis process, CoFe₂O₄ nanoparticles were first synthesized by a coprecipitation method, and then transformed into the FeS₂ and CoS₂ phases. During the latter sulfuration process, interfaces with defect sites were created in the FeS₂/CoS₂ NSs. Electron paramagnetic resonance (EPR) spectra revealed a stronger EPR signal at $g = 2.007$ recorded with the FeS₂/CoS₂ NSs composite, indicating abundant S vacancies. Extended X-ray absorption fine structure (EXAFS) was used to further investigate the local structure of the obtained samples, and a distinct decrease in peak intensity in Fe K-edge EXAFS was detected with FeS₂/CoS₂ NSs, demonstrating the coordination deficiency from Fe. Similar results were reported by Gao et al. [279] in CeO₂/NiO with an embedded configuration

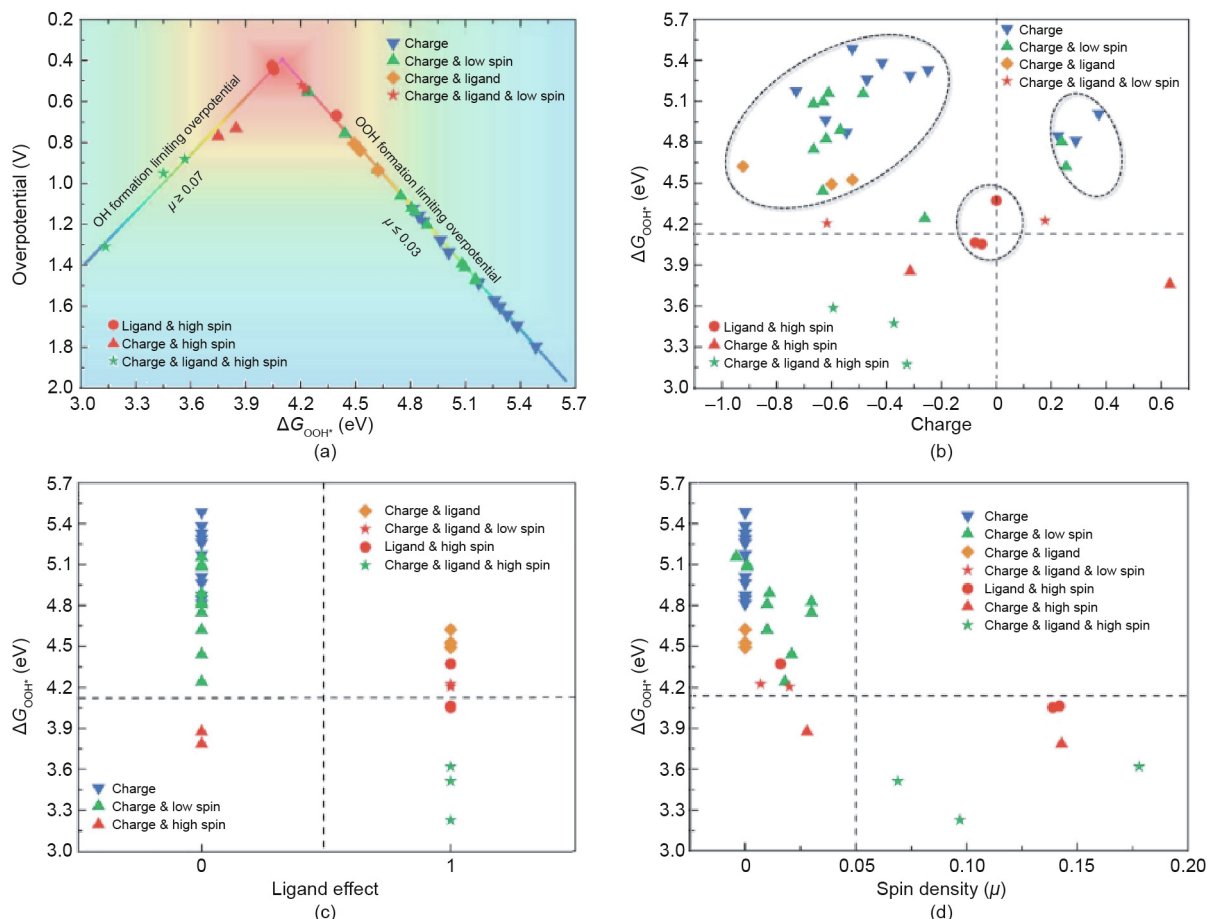


Fig. 17. (a) ORR overpotential as a function of ΔG_{OOH^*} for carbon active sites. ΔG_{OOH^*} vs (b) charge effect, (c) ligand effect, and (d) spin density effect. Reproduced from Ref. [248] with permission of The Royal Society of Chemistry, ©2018.

(Ce–NiO–E) or the surface-loaded configuration (Ce–NiO–L). An increasing trend of Ni^{3+} and oxygen defects for NiO (Ni^{3+} 62%, O defect 24%), Ce–NiO–L (Ni^{3+} 69%, O defect 26%), and Ce–NiO–E (Ni^{3+} 71%, O defect 32%) correlated well with the activity trend, indicating that these vacancy sites at the interface region contribute greatly to the enhanced activity. In fact, electron modulation and vacancy do not exist independently, and the catalytic performances of the interfaced materials may be influenced by the two factors simultaneously.

3.8. Alloying

Alloying is the diffusion penetration of the metal atoms of two or more metals, or the addition of nonmetallic elements into metals through melting, sintering, or vapor deposition processes. Metal alloying is an effective strategy for improving the performance of metal catalysts. It can not only refine the grain size to improve the mechanical strength and surface area of catalysts, but also selectively reduce the amount of a single component (e.g., Pt, Au, Ru, and other precious metals) in order to reduce the catalyst cost. Moreover, the catalytic activity and selectivity of metals can be changed by incorporating other metals to form alloys, due to the synergistic effect between metal components [280–284]

According to the Brewer–Engel valence bond theory [285], alloying a metal with an unfilled d orbital and a metal with internally paired d-electrons can modulate the hydrogen adsorption energy on the alloy surface, thus improving the hydrogen evolution activity. Raj [286] prepared a series of Ni-based binary composites by means of electrodeposition techniques. The trend in their HER activities in alkaline water followed this order: Ni–Mo > Ni–Zn >

Ni–Co > Ni–W > Ni–Fe > Ni–Cr. Due to its excellent activity, the Ni–Mo alloy has been considered to be the most promising HER catalytic material. Zhang et al. [287] successfully constructed a layer of Ni–Mo alloy nanorods with uniform size and uniform element distribution on the surface of a nickel substrate by means of magnetron sputtering technology, and found that the HER exchange current density was almost ten times higher than that of single-metal Ni or Mo catalysts. This research showed that the excellent catalytic activity of the Ni–Mo alloy electrode mainly comes from two factors: ① There is an increase in the specific surface, caused by the grain refinement of the two-component metal in the growth process; and ② the electronegativity difference between the elements Ni and Mo causes electrons to concentrate around Mo, thus forming a synergy for electrocatalysis.

In order to reduce the usage of precious metals, many non-noble metals (i.e., Co, Ni, Fe, Cu, V, Cr, Mn, Zn, etc.) have been incorporated with noble metals to form alloys as electrocatalysts [206,288]. Studies of ORR performances on PtM alloys revealed the following activity order [289–291]: PtFe/C > PtCo/C > PtV/C > PtNi/C > Pt/C. The following stability order was also determined [292]: Pt₃Ir(111) > Pt₃Co(111) > Pt₃Ni(111) > Pt₃Fe(111). In addition, Greeley et al. [293] found a classic volcano-shaped dependency based on the ORR activity of Pt alloys versus the d-band center position of 3d metals (Fig. 20). According to that study, the ORR mechanism on Pt₃M catalysts was either O₂ dissociation or proton/electron transfer to molecular O₂, and the optimal ORR catalyst should have a weaker oxygen-binding energy than Pt. Bampos et al. [294] further synthesized a series of carbon-supported Pd–M (where M = Ag, Co, Cu, Fe, Ni, or Zn) bimetallic

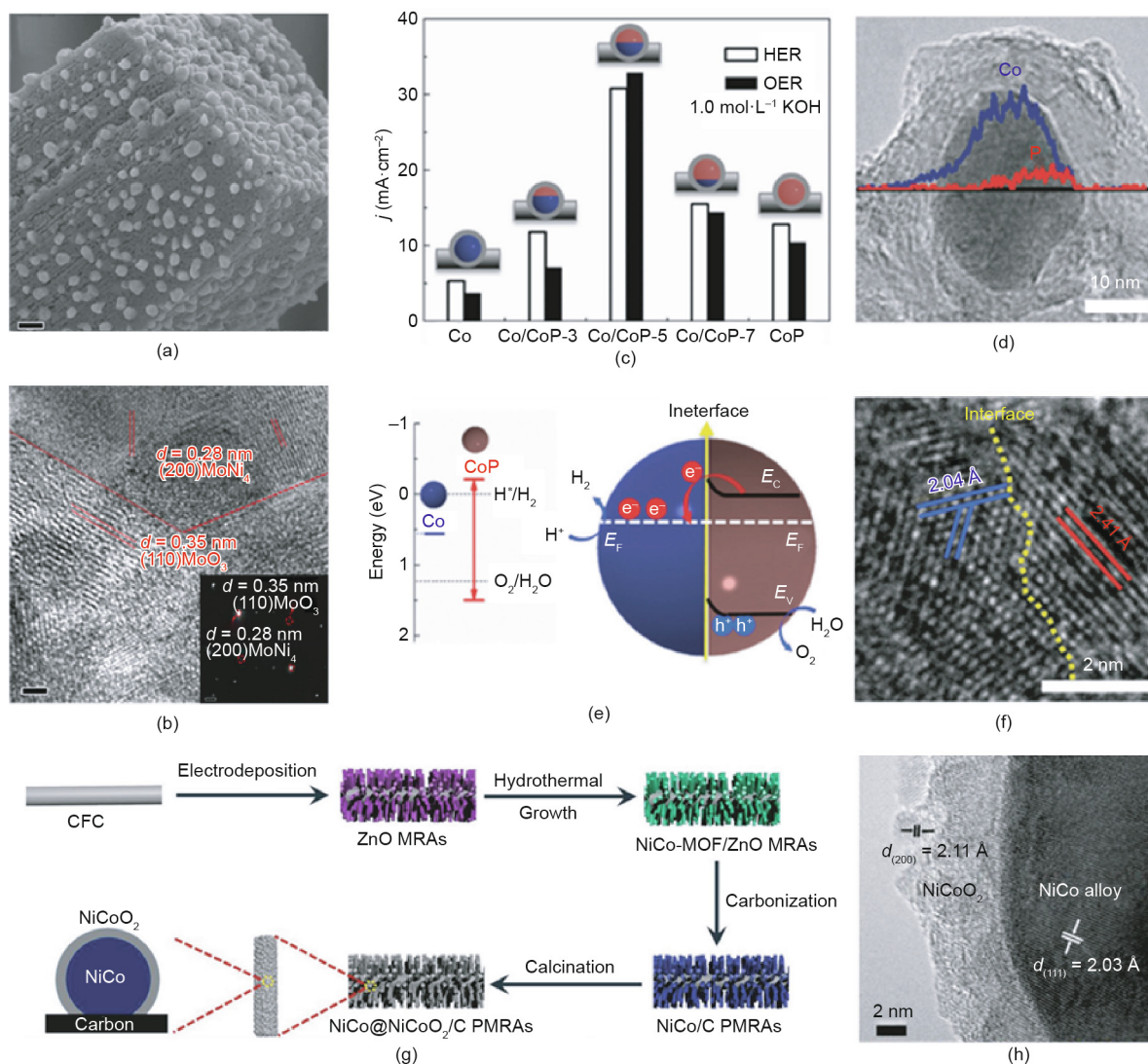


Fig. 18. (a, b) Typical SEM images of MoNi₄/MoO₂@Ni; (c) current densities of the obtained samples; (d) compositional line profile of a typical Co/CoP-5 nanoparticle; (e) electronic structures of metallic Co and CoP, and the Co/CoP-based Mott-Schottky contact; (f) HRTEM image of a typical Co/CoP-5 nanoparticle; (g) fabrication process and (h) HRTEM image of NiCo@NiCoO₂/C PMRAs. CFC: carbon fiber cloth; MRA: microrod arrays. Reproduced from Ref. [259] with permission of WILEY-VCH Verlag GmbH & Co. KGaA, ©2018.

catalysts as ORR electrocatalysts in acidic solution. The ORR activity of these Pd-based alloys was found to descend as follows: PdZn/C > PdNi/C > Pt/C > PdAg/C ≥ PdCo/C > PdFe/C > PdCu/C > Pd/C. Notably, PdZn/C exhibited a specific activity three times higher than Pt/C at a potential between 0.35 and 0.5 V versus Ag/AgCl.

In addition to metallic elements, the introduction of nonmetallic elements can improve the catalytic performance of alloys [295–299]. For example, Kiran et al. [296] prepared few-layer MoS₂(1-x)Se_{2x} alloys that possessed higher HER activity than pristine MoS₂ and MoSe₂. A systematic structure-activity relationship was revealed by tuning the Se/S incorporation in MoS₂(1-x)Se_{2x} with MoS_{1.0}Se_{1.0} having an Se/S ratio of 1:1 showing the highest HER activity. Similar results regarding Mo–S–Se alloys were reported by the groups of Gong et al. [299] and Xu et al. [297]. Xu et al. [298] successfully controlled the composition of sulfur (S) and selenium (Se) in ternary WS₂(1-x)Se_{2x} nanotubes on carbon fibers. The disordered atom arrangement introduced in the alloyed structure resulted in WS₂(1-x)Se_{2x} having excellent electrocatalytic properties for HER. A ternary pyrite-type CoPS was further obtained by Cabán-Acevedo et al. [300] for photo/electrochemical hydrogen evolution. Because of the higher electron-donating char-

acter of the P²⁻ ligands in CoPS, this ternary pyrite CoPS was endowed with a more thermoneutral hydrogen adsorption, resulting in a higher HER activity than CoS₂.

4. Conclusions and perspectives

The majority of the energy dissipation in electrochemical hydrogen–water conversion is induced by the activation energy driving the electrochemical reactions involved in the energy system. Materials are at the core of a high-efficiency energy system, as the activation energy of the reactions involved in the system is strongly influenced by the catalytic materials. It is urgent to accelerate the development of active and robust electrocatalysts with acceptable cost in order to ensure that an efficient and sustainable energy system becomes a reality. In general, a catalyst's performance depends on two main factors: ① the number of active sites in a given area; and ② the intrinsic activity of each active site. Tuning the geometric structure (i.e., the nanoarchitecture and facet engineering) makes it possible to realize enhancement of the active sites, because when the catalyst size is reduced to the nanoscale,

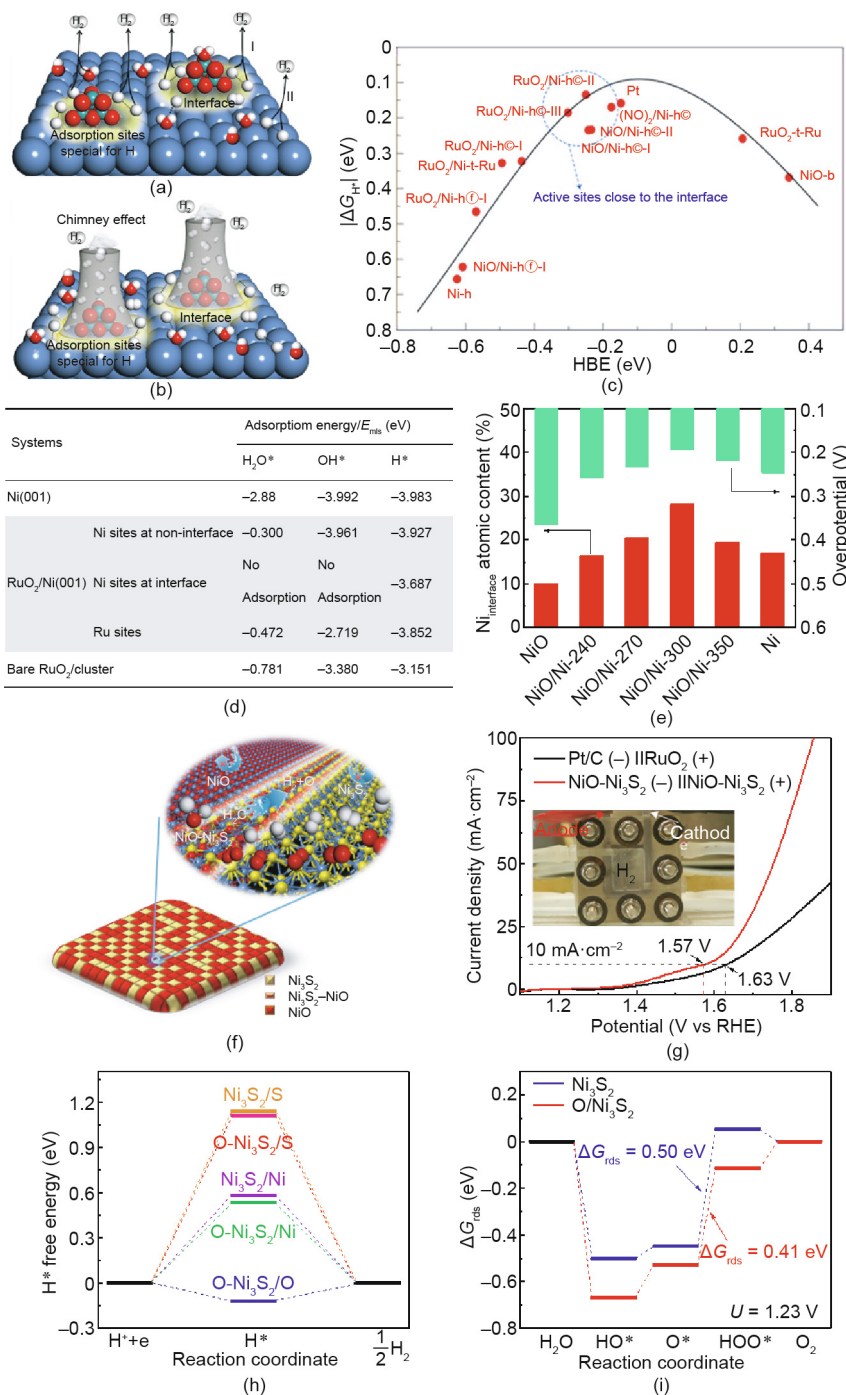


Fig. 19. (a) Schematic diagrams of two possible HER pathways on RuO₂/Ni composite catalysts; (b) a "chimney effect" at the metal/metal oxide interface; (c) the curve of ΔG_{H^+} vs HBE (hydrogen binding energy); (d) adsorption energy of H₂O*, OH*, and H* species on different clusters; (e) variation trend of the Ni_{interface} content and the HER activities of NiO/Ni samples; (f) schematic of water electrolysis catalyzed by monometallic NiO–Ni₃S₂ heteronanosheets; (g) polarization curves of the NiO–Ni₃S₂ couple or Pt/C and RuO₂ electrode couple for water electrolysis; (h) hydrogen free energy and (i) OER free-energy diagrams over Ni₃S₂ and O–Ni₃S₂ surfaces. (a–e) reproduced from Ref. [270] with permission of Elsevier B.V., ©2019; (f–i) reproduced from Ref. [271] with permission of Elsevier Inc., ©2019.

the catalyst possesses a high surface area with increased exposure of the catalytically active planes. Defect engineering and amorphization can also be applied to enrich active sites by exposing thermodynamically unstable active sites or active unsaturated atoms. Increasing the intrinsic activity of the active site is a more fundamental yet difficult strategy for activity improvement, which involves accurate modulation of the electronic structures of catalytic materials. Optimization of the intrinsic activity can be achieved based on a fundamental understanding of the particularities of the reactions and insight into the design of catalysts with

targeted functionalities. The featured examples (their catalytic performances are summarized in Tables 2–5) discussed herein present successful modulation of the intrinsic activity via element doping, interface engineering, polymorph engineering, alloying, and so forth, with the aid of synergistic interaction between theoretical and experimental studies.

At present, with the rapid development of chemical synthesis techniques, many catalytic materials have been reported with outstanding electrocatalytic performance. Meanwhile, developments in physical characterization methods and theoretical calculation

Table 3
Summary of electrocatalysts' performance in OER.

OER catalyst	Electrolyte	η^{10} (mV)	Tafel slope (mV-decade ⁻¹)	Ref.
Co–Pi NA/Ti	0.1 mol·L ⁻¹ PBS	450	187	[81]
NiSe/NF	1 mol·L ⁻¹ KOH	270 ²⁰	64	[83]
NiCo ₂ (SOH) _x /NF	1 mol·L ⁻¹ NaOH	290	47	[94]
FeNi(OH) _x /Ni	1 mol·L ⁻¹ KOH	254 ⁵⁰	45	[95]
Co ₃ O ₄ /N-rGO	0.1 mol·L ⁻¹ KOH	380	62	[161]
SC CoO NRs	1 mol·L ⁻¹ KOH	330	44	[165]
Mono-NiTi-MMO	1 mol·L ⁻¹ KOH	320	52	[167]
Fe ₆ Ni ₁₀ O _x	1 mol·L ⁻¹ KOH	286	48	[186]
CoFe ₂ O _n	0.1 mol·L ⁻¹ KOH	490	48	[188]
Co ₃ O ₄ films	0.1 mol·L ⁻¹ KPi	–	65	[189]
DG	1 mol·L ⁻¹ KOH	340	97	[222]
Fe–CoP/Ti	1 mol·L ⁻¹ KOH	230	67	[223]
Co _{1–x} Fe _x P/CNT	1 mol·L ⁻¹ KOH	243	30	[224]
N,P-GCNS	0.1 mol·L ⁻¹ KOH	340	–	[247]
Co/CoP-5	1 mol·L ⁻¹ KOH	340	79.5	[258]
NiCo@NiCoO ₂ /C PMRAs	1 mol·L ⁻¹ KOH	366 ²⁰	83.97	[259]
Ni(OH) ₂ –CeO ₂	1 mol·L ⁻¹ KOH	220	81.9	[262]
Fe ₃ O ₄ @Co ₉ S ₈ /rGO	1 mol·L ⁻¹ KOH	340	54.4	[263]
Co–Mo ₂ C NPs	0.1 mol·L ⁻¹ KOH	347	38	[267]
NiO–Ni ₃ S ₂	1 mol·L ⁻¹ KOH	290 ²⁰	75	[271]
CoSe/FeSe ₂	1 mol·L ⁻¹ KOH	246	41.4	[274]
Co–Ni ₃ N	1 mol·L ⁻¹ KOH	307	57	[277]
Ce–NiO–E	1 mol·L ⁻¹ KOH	382	118.7	[279]

GCNS: graphene/carbon nanosheets; MMO: mixed metal oxide.

Table 4
Summary of non-noble metal electrocatalysts' performance in ORR.

Non-noble ORR catalyst	Electrolyte	E_{onset} (V)	$E_{1/2}$ (V)	Ref.
Fe-NMCSs	0.1 mol·L ⁻¹ KOH	1.027	0.86	[104]
VB12/Silica colloid	0.5 mol·L ⁻¹ H ₂ SO ₄	–	0.79	[105]
Fe/N/CF	0.5 mol·L ⁻¹ H ₂ SO ₄	0.93	0.80	[108]
Fe,N-OMC	0.1 mol·L ⁻¹ KOH	0.99	–	[110]
Co-N-OMMC-0.6	0.1 mol·L ⁻¹ KOH	–	0.83	[111]
FeN ₂ /NOMC	0.1 mol·L ⁻¹ KOH	1.05	0.863	[112]
NH ₃ –Fe _{0.25} –N/C-900	0.1 mol·L ⁻¹ KOH	1.018	0.865	[113]
Meso/micro-PoPD	0.1 mol·L ⁻¹ KOH	–	0.85	[118]
O-NCNT	0.1 mol·L ⁻¹ KOH	1.052	0.885	[121]
Co ₃ O ₄ -NP/N-rGO	0.1 mol·L ⁻¹ KOH	0.89	0.76	[161]
SC CoO NRs	1 mol·L ⁻¹ KOH	0.96	0.85	[165]
{Co}[FeCo]O ₄ /NG	0.1 mol·L ⁻¹ KOH	0.98	0.866	[176]
CoFe ₂ O _n	0.1 mol·L ⁻¹ KOH	0.80	–	[188]
CNC700	0.1 mol·L ⁻¹ KOH	~0.099 (vs Ag/AgCl)	–	[219]
PC-18-950	0.1 mol·L ⁻¹ KOH	–0.06 (vs Ag/AgCl)	–0.25 (vs Ag/AgCl)	[221]
DG	0.1 mol·L ⁻¹ KOH	0.91	0.76	[222]
N,P-GCNS	0.1 mol·L ⁻¹ KOH	1.01	0.86	[247]

CF: carbon nanofibrous; MCSs: mesoporous carbon microspheres; NCNT: nitrogen-doped carbon; Nanotube; OMC: Ordered mesoporous carbons; OMMC: ordered macro-/mesoporous carbon; PoPD: porous N-doped carbon.

Table 5
Summary of noble-metal electrocatalysts' performance in ORR.

Noble ORR catalyst	Electrolyte	Specific activity (mA·cm ⁻²)	Mass activity (A·mg _{Pt} ⁻¹)	Ref.
Pt octahedra	0.1 mol·L ⁻¹ HClO ₄	1.50	0.25	[147]
Pd ₃ Pb TP/C	0.1 mol·L ⁻¹ KOH	1.76	0.56 _{Pd}	[148]
PdCu B ₂ @Pt–Cu/C	0.1 mol·L ⁻¹ HClO ₄	4.33	2.55	[149]
Au@Pd@Pt TOHs	0.1 mol·L ⁻¹ HClO ₄	1.165	0.97	[157]
PtCu OFAs	0.1 mol·L ⁻¹ HClO ₄	5.98	3.26	[158]
Pt-skin Pt ₃ Fe z-NWs	0.1 mol·L ⁻¹ HClO ₄	4.34	2.11	[159]
Pd–Cu/Vulcan	0.1 mol·L ⁻¹ KOH	1.27	0.59 _{Pd}	[282]

OFA: octopod nanoframe architectures; TOH: trisoctahedrons.

actual reaction process of the catalytic material surface. Furthermore, although the reaction mechanisms of these hydrogen- and oxygen-involving reactions have been widely investigated, the actual mechanisms on different catalyst surfaces remain shrouded in mystery. In fact, it is also difficult to identify the actual active sites, as the surface structure of most catalysts varies during the electrocatalytic process. New progress will come from the merging

of advanced theoretical calculations and experimental characterization (e.g., *in situ*, *ex situ*, and *operando* techniques), which will allow us to promote our understanding of the electrochemical reaction mechanism and the dynamic evolution of the catalysts involved at the molecular level. Finally, function-oriented catalyst preparation remains a major challenge. Existing material synthesis technologies are able to regulate the physical and chemical

properties of specific catalysts to some extent at the nanoscale, but the use of controlled synthesis technology to modulate the electronic structure of catalysts at the atomic scale remains immature. The development of controllable synthesis methods with strong applicability and large-scale production is another focus of future research.

Acknowledgements

We gratefully acknowledge financial support from the National Natural Science Foundation of China (21576032 and 51772037), the Key Program of the National Natural Science Foundation of China (21436003), the Major Research Plan of the National Natural Science Foundation of China (91534205), and the National Program on Key Basic Research Project of China (2016YFB0101202).

Compliance with ethics guidelines

Lishan Peng and Zidong Wei declare that they have no conflict of interest or financial conflicts to disclose.

Nomenclature

c	reactant surface concentration, $\text{mol}\cdot\text{m}^{-3}$
F	Faraday constant, $\sim 96\,485\text{ C}\cdot\text{mol}^{-1}$
G	Gibbs free energy, $\text{J}\cdot\text{mol}^{-1}$
f	decay rate to products and reactants, dimensionless
i	current, A
j	current density, $\text{A}\cdot\text{cm}^{-2}$
j_0	exchange current density, $\text{A}\cdot\text{cm}^{-2}$
n	number of electrons transferred in the reaction, dimensionless
R	resistance, Ω
T	temperature, K
U_0	reaction equilibrium potential, V
V	voltage, V
α	charge transfer coefficient, dimensionless
μ	overvoltage, V
ΔG_{act}	activation energy barrier, $\text{J}\cdot\text{mol}^{-1}$
ΔG_{H^+}	hydrogen adsorption free energy
ΔG_{max}	gibbs free-energy change, $\text{J}\cdot\text{mol}^{-1}$
ΔG_{O^+}	oxygen adsorption strength

References

- Chen P, Zhu M. Recent progress in hydrogen storage. *Mater Today* 2008;11(12):36–43.
- Peng L, Wei Z. Design and product engineering of high-performance electrode catalytic materials for water electrolysis. *Prog Chem* 2018;30(1):14–28.
- Liu Y. Progress of green energy hydrogen energy and technology of hydrogen production by water electrolysis. *Chin J Powder Sources* 2012;36(10):1579–81. Chinese.
- Mueller-Langer F, Tzimas E, Kaltschmitt M, Peteves S. Techno-economic assessment of hydrogen production processes for the hydrogen economy for the short and medium term. *Int J Hydrogen Energy* 2007;32(16):3797–810.
- Kothari R, Buddhi D, Sawhney RL. Comparison of environmental and economic aspects of various hydrogen production methods. *Renew Sustain Energy Rev* 2008;12(2):553–63.
- National Research Council. The hydrogen economy: opportunities, costs, barriers, and R&D needs. Washington, DC: The National Academies Press; 2004.
- Barreto L, Makihiro A, Riahi K. The hydrogen economy in the 21st century: a sustainable development scenario. *Int J Hydrogen Energy* 2003;28(3):267–84.
- Tromp TK, Shia RL, Allen M, Eiler JM, Yung YL. Potential environmental impact of a hydrogen economy on the stratosphere. *Science* 2003;300(5626):1740–2.
- Crabtree GW, Dresselhaus M, Buchanan M. The hydrogen economy. *Phys Today* 2004;57(12):39–44.
- Yan ZY, Kong XW. Research on non-grid-connected wind power water-electrolytic hydrogen production system and its applications. *Eng Sci* 2015(3):30–4. Chinese.
- Holladay JD, Hu J, King DL, Wang Y. An overview of hydrogen production technologies. *Catal Today* 2009;139(4):244–60.
- Zhang WQ, Yu B, Chen J, Xu JM. Hydrogen production through solid oxide electrolysis at elevated temperatures. *Prog Chem* 2008;20(5):778–87.
- Yu H, Yi B. Hydrogen for energy storage and hydrogen production from electrolysis. *Strategic Study Chin Acad Eng* 2018;20(3):58–65.
- Penner SS. Steps toward the hydrogen economy. *Energy* 2006;31(1):33–43.
- Marbán G, Valdés-Solís T. Towards the hydrogen economy? *Int J Hydrogen Energy* 2007;32(12):1625–37.
- Dresselhaus MS. Basic research needs for the hydrogen economy. In: *Proceedings of American Physical Society March Meeting 2004*; 2004 Mar 22–26; Montreal, QB, Canada; 2004.
- Armor JN. Catalysis and the hydrogen economy. *Catal Lett* 2005;101(3–4):131–5.
- Vlachos DG, Caratzoulas S. The roles of catalysis and reaction engineering in overcoming the energy and the environment crisis. *Chem Eng Sci* 2010;65(1):18–29.
- Farrauto RJ. New catalysts and reactor designs for the hydrogen economy. *Chem Eng J* 2014;238:172–7.
- Wang J, Wang H, Fan Y. Techno-economic challenges of fuel cell commercialization. *Engineering* 2018;4(3):352–60.
- Wu G. Current challenge and perspective of PGM-free cathode catalysts for PEM fuel cells. *Front Energy* 2017;11(3):286–98.
- Wang YQ, Zhang JT. Structural engineering of transition metal-based nanostructured electrocatalysts for efficient water splitting. *Front Chem Sci Eng* 2018;12(4):838–54.
- Peng LS, Wei ZD. Recent progress of mesoscience in design of electrocatalytic materials for hydrogen energy conversion. *Particuology* 2020;48:19–33.
- Zeng K, Zhang D. Recent progress in alkaline water electrolysis for hydrogen production and applications. *Prog Energy Combust Sci* 2010;36(3):307–26.
- Wolfschmidt H, Paschos O, Stimming U. Fuel cell science: theory, fundamentals, and biocatalysis. Hoboken: John Wiley & Sons, Inc; 2010.
- Trasatti S. Electrodes of conductive metallic oxides. Amsterdam: Elsevier Scientific Software; 1980.
- Nie Y, Li L, Wei Z. Recent advancements in Pt and Pt-free catalysts for oxygen reduction reaction. *Chem Soc Rev* 2015;44(8):2168–201.
- Peng LS, Syed SSA, Wei ZD. Recent developments in metal phosphide and sulfide electrocatalysts for oxygen evolution reaction. *Chin J Catal* 2018;39(10):1575–93.
- Seh ZW, Kibsgaard J, Dickens CF, Chorkendorff I, Nørskov JK, Jaramillo TF. Combining theory and experiment in electrocatalysis: insights into materials design. *Science* 2017;355(6321):eaad4998.
- Jiao Y, Zheng Y, Jaroniec M, Qiao SZ. Design of electrocatalysts for oxygen- and hydrogen-involving energy conversion reactions. *Chem Soc Rev* 2015;44(8):2060–86.
- Rozain C, Millet P. Electrochemical characterization of polymer electrolyte membrane water electrolysis cells. *Electrochim Acta* 2014;131:160–7.
- Brug GJ, van den Eeden ALG, Sluyters-Rehbach M, Sluyters JH. The analysis of electrode impedances complicated by the presence of a constant phase element. *J Electroanal Chem Interfacial Electrochem* 1984;176(1–2):275–95.
- Belmont C, Girault HH. Coplanar interdigitated band electrodes for synthesis part I: ohmic loss evaluation. *J Appl Electrochem* 1994;24(6):475–80.
- Bard AJ, Faulkner LR. *Electrochemical methods: fundamentals and applications*. New York: John Wiley & Sons, Inc; 1980.
- Bird RB, Stewart WE, Lightfoot EN. *Transport phenomena*. 2nd ed. New York: John Wiley & Sons, Inc; 2007.
- Oldham KB, Myland JC. *Fundamentals of electrochemical science*. San Diego: Academic Press; 1994.
- Wen CY, Lin YS, Lu CH. Experimental study of clamping effects on the performances of a single proton exchange membrane fuel cell and a 10-cell stack. *J Power Sources* 2009;192(2):475–85.
- Huang J, Li Z, Zhang JB. Review of characterization and modeling of polymer electrolyte fuel cell catalyst layer: the blessing and curse of ionomer. *Front Energy* 2017;11(3):334–64.
- Godula-Jopek A, editor. *Hydrogen production: electrolysis*. Weinheim: Wiley-VCH; 2015.
- O'hayre R, Cha SW, Colella WG, Prinz FB. *Fuel cell fundamentals*. Hoboken: John Wiley & Sons, Inc; 2016.
- Hine F, Murakami K. Bubble effects on the solution IR drop in a vertical electrolyzer under free and forced-convection. *J Electrochem Soc* 1980;127(2):292–7.
- Crow DR. *Principles and applications of electrochemistry*. 3rd ed. London: Chapman and Hall; 1988.
- Pickett DJ. *Electrochemical reactor design*. Amsterdam: Elsevier Scientific Publishing Company; 1979.
- Dyer CK. Improved nickel anodes for industrial water electrolyzers. *J Electrochem Soc* 1985;132(1):64–7.
- Kinoshita K. *Electrochemical oxygen technology*. New York: John Wiley & Sons, Inc; 1992.
- Mueller U, Schubert M, Yaghi O, Ertl G, Knözinger H, Schüth F, et al. *Handbook of heterogeneous catalysis 2008*; vol. 1:247–62.
- Newman J, Thomas-Alyea KE. *Electrochemical systems*. 3rd ed. Hoboken: John Wiley & Sons, Inc; 2012.
- Horiuti J, Polanyi M. Grundlinien einer theorie der protonübertragung. *Acta Physicochim URSS* 1935;2(4):505–32.

- [49] Sheng WC, Gasteiger HA, Shao-Horn Y. Hydrogen oxidation and evolution reaction kinetics on platinum: acid vs alkaline electrolytes. *J Electrochem Soc* 2010;157(11):B1529–36.
- [50] Bockris JOM, Potter EC. The mechanism of the cathodic hydrogen evolution reaction. *J Electrochem Soc* 1952;99(4):169–86.
- [51] Parsons R. The rate of electrolytic hydrogen evolution and the heat of adsorption of hydrogen. *Trans Faraday Soc* 1958;54:1053–63.
- [52] Xiang R, Peng LS, Wei ZD. Tuning interfacial structures for better catalysis of water electrolysis. *Chem Eur J* 2019;25(42):9799–815.
- [53] Peng LS, Liao MS, Zheng XQ, Nie Y, Zhang L, Wang MJ, et al. Accelerated alkaline hydrogen evolution on $M(OH)_x/M-MoPO_x$ ($M = Ni, Co, Fe, Mn$) electrocatalysts by coupling water dissociation and hydrogen ad-desorption steps. *Chem Sci* 2020;11(9):2487–93.
- [54] Zheng Y, Jiao Y, Zhu Y, Li LH, Han Y, Chen Y, et al. Hydrogen evolution by a metal-free electrocatalyst. *Nat Commun* 2014;5(1):3783.
- [55] Liu P, Rodriguez JA. Catalysts for hydrogen evolution from the [NiFe]. Hydrogenase to the $Ni_2P(001)$ surface: the importance of ensemble effect. *J Am Chem Soc* 2005;127(42):14871–8.
- [56] Esposito DV, Hunt ST, Kimmel YC, Chen JG. A new class of electrocatalysts for hydrogen production from water electrolysis: metal monolayers supported on low-cost transition metal carbides. *J Am Chem Soc* 2012;134(6):3025–33.
- [57] Shao M. Palladium-based electrocatalysts for hydrogen oxidation and oxygen reduction reactions. *J Power Sources* 2011;196(5):2433–44.
- [58] Nørskov JK, Bligaard T, Logadottir A, Kitchin JR, Chen JG, Pandalov S, et al. Trends in the exchange current for hydrogen evolution. *J Electrochem Soc* 2005;152(3):J23–6.
- [59] Greeley J, Nørskov JK, Kibler LA, El-Aziz AM, Kolb DM. Hydrogen evolution over bimetallic systems: understanding the trends. *ChemPhysChem* 2006;7(5):1032–5.
- [60] Trasatti S. Work function, electronegativity, and electrochemical behaviour of metals: III. electrolytic hydrogen evolution in acid solutions. *J Electroanal Chem Interfacial Electrochem* 1972;39(1):163–84.
- [61] Durst J, Simon C, Siebel A, Rheinlander JP, Schuler T, Hanzlik M, et al. Hydrogen oxidation and evolution reaction (HOR/HER) on Pt electrodes in acid vs. alkaline electrolytes: mechanism, activity and particle size effects. *ECS Trans* 2014;64(3):1069–80.
- [62] Siahrostami S, Verdager-Casadevall A, Karamad M, Deiana D, Malacrida P, Wickman B, et al. Enabling direct H_2O_2 production through rational electrocatalyst design. *Nat Mater* 2013;12(12):1137–43.
- [63] Nørskov JK, Rossmeisl J, Logadottir A, Lindqvist L, Kitchin JR, Bligaard T, et al. Origin of the overpotential for oxygen reduction at a fuel-cell cathode. *J Phys Chem B* 2004;108(46):17886–92.
- [64] Greeley J, Nørskov JK. Combinatorial density functional theory-based screening of surface alloys for the oxygen reduction reaction. *J Phys Chem C* 2009;113(12):4932–9.
- [65] Viswanathan V, Hansen HA, Rossmeisl J, Nørskov JK. Unifying the $2e^-$ and $4e^-$ reduction of oxygen on metal surfaces. *J Phys Chem Lett* 2012;3(20):2948–51.
- [66] Hansen HA, Viswanathan V, Nørskov JK. Unifying kinetic and thermodynamic analysis of $2e^-$ and $4e^-$ reduction of oxygen on metal surfaces. *J Phys Chem C* 2014;118(13):6706–18.
- [67] Trasatti S. Electrocatalysis in the anodic evolution of oxygen and chlorine. *Electrochim Acta* 1984;29(11):1503–12.
- [68] Rossmeisl J, Logadottir A, Nørskov JK. Electrolysis of water on (oxidized) metal surfaces. *Chem Phys* 2005;319(1–3):178–84.
- [69] Rossmeisl J, Qu ZW, Zhu H, Kroes GJ, Nørskov JK. Electrolysis of water on oxide surfaces. *J Electroanal Chem (Lausanne Switz)* 2007;607(1–2):83–9.
- [70] Man IC, Su HY, Calle-Vallejo F, Hansen HA, Martínez JI, Inoglu NG, et al. Universality in oxygen evolution electrocatalysis on oxide surfaces. *ChemCatChem* 2011;3(7):1159–65.
- [71] Koper MTM. Thermodynamic theory of multi-electron transfer reactions: implications for electrocatalysis. *J Electroanal Chem (Lausanne Switz)* 2011;660(2):254–60.
- [72] Viswanathan V, Hansen HA, Rossmeisl J, Nørskov JK. Universality in oxygen reduction electrocatalysis on metal surfaces. *ACS Catal* 2012;2(8):1654–60.
- [73] Vojvodic A, Nørskov JK. New design paradigm for heterogeneous catalysts. *Natl Sci Rev* 2015;2(2):140–3.
- [74] Pedersen CM, Escudero-Escribano M, Velázquez-Palenzuela A, Christensen LH, Chorkendorff I, Stephens IEL. Benchmarking Pt-based electrocatalysts for low temperature fuel cell reactions with the rotating disk electrode: oxygen reduction and hydrogen oxidation in the presence of CO. *Electrochim Acta* 2015;179:647–57.
- [75] Sabatier P. Hydrogénations et déshydrogénations par catalyse. *Ber Dtsch Chem Ges* 1911;44(3):1984–2001. German.
- [76] Li X, Hao X, Abudula A, Guan G. Nanostructured catalysts for electrochemical water splitting: current state and prospects. *J Mater Chem A* 2016;4(31):11973–2000.
- [77] Morales-Guio CG, Stern LA, Hu X. Nanostructured hydrotreating catalysts for electrochemical hydrogen evolution. *Chem Soc Rev* 2014;43(18):6555–69.
- [78] Fang M, Dong G, Wei R, Ho JC. Hierarchical nanostructures: design for sustainable water splitting. *Adv Energy Mater* 2017;7(23):1700559.
- [79] Liu R, Duay J, Lee SB. Heterogeneous nanostructured electrode materials for electrochemical energy storage. *Chem Commun (Camb)* 2011;47(5):1384–404.
- [80] Tang C, Zhang R, Lu W, Wang Z, Liu D, Hao S, et al. Energy-saving electrolytic hydrogen generation: Ni_2P nanoarray as a high-performance non-noble-metal electrocatalyst. *Angew Chem Int Ed Engl* 2017;56(3):842–6.
- [81] Xie L, Zhang R, Cui L, Liu D, Hao S, Ma Y, et al. High-performance electrolytic oxygen evolution in neutral media catalyzed by a cobalt phosphate nanoarray. *Angew Chem Int Ed Engl* 2017;56(4):1064–8.
- [82] Ji Y, Yang L, Ren X, Cui G, Xiong X, Sun X. Nanoporous CoP_3 nanowire array: acid etching preparation and application as a highly active electrocatalyst for the hydrogen evolution reaction in alkaline solution. *ACS Sustain Chem Eng* 2018;6(9):11186–9.
- [83] Tang C, Cheng N, Pu Z, Xing W, Sun X. NiSe nanowire film supported on nickel foam: an efficient and stable 3D bifunctional electrode for full water splitting. *Angew Chem Int Ed Engl* 2015;54(32):9351–5.
- [84] Wang J, Cui W, Liu Q, Xing Z, Asiri AM, Sun X. Recent progress in cobalt-based heterogeneous catalysts for electrochemical water splitting. *Adv Mater* 2016;28(2):215–30.
- [85] Brown DE, Mahmood MN, Turner AK, Hall SM, Fogarty PO. Low overvoltage electrocatalysts for hydrogen evolving electrodes. *Int J Hydrogen Energy* 1982;7(5):405–10.
- [86] Navarro-Flores E, Chong ZW, Omanovic S. Characterization of Ni, NiMo, NiW and NiFe electroactive coatings as electrocatalysts for hydrogen evolution in an acidic medium. *J Mol Catal Chem* 2005;226(2):179–97.
- [87] McKone JR, Sadtler BF, Werlang CA, Lewis NS, Gray HB. Ni-Mo nanopowders for efficient electrochemical hydrogen evolution. *ACS Catal* 2013;3(2):166–9.
- [88] Gao MR, Xu YF, Jiang J, Yu SH. Nanostructured metal chalcogenides: synthesis, modification, and applications in energy conversion and storage devices. *Chem Soc Rev* 2013;42(7):2986–3017.
- [89] Faber MS, Jin S. Earth-abundant inorganic electrocatalysts and their nanostructures for energy conversion applications. *Energy Environ Sci* 2014;7(11):3519–42.
- [90] Mai L, Tian X, Xu X, Chang L, Xu L. Nanowire electrodes for electrochemical energy storage devices. *Chem Rev* 2014;114(23):11828–62.
- [91] Carenco S, Portehault D, Boissière C, Mézailles N, Sanchez C. Nanoscaled metal borides and phosphides: recent developments and perspectives. *Chem Rev* 2013;113(10):7981–8065.
- [92] Faber MS, Dziedzic R, Lukowski MA, Kaiser NS, Ding Q, Jin S. High-performance electrocatalysis using metallic cobalt pyrite (CoS_2) micro- and nanostructures. *J Am Chem Soc* 2014;136(28):10053–61.
- [93] Peng LS, Nie Y, Zhang L, Xiang R, Wang J, Chen HM, et al. Self-assembly- and preshaping-assisted synthesis of molybdenum carbide supported on ultrathin nitrogen-doped graphitic carbon lamellas for the hydrogen evolution reaction. *ChemCatChem* 2017;9(9):1588–93.
- [94] Peng LS, Wang J, Nie Y, Xiong K, Wang Y, Zhang L, et al. Dual-ligand synergistic modulation: a satisfactory strategy for simultaneously improving the activity and stability of oxygen evolution electrocatalysts. *ACS Catal* 2017;7(12):8184–91.
- [95] Xiang R, Tong C, Wang Y, Peng LS, Nie Y, Li L, et al. Hierarchical coral-like $FeNi(OH)_x/Ni$ via mild corrosion of nickel as an integrated electrode for efficient overall water splitting. *Chin J Catal* 2018;39(11):1736–45.
- [96] Peng LS, Shen JJ, Zhang L, Wang Y, Xiang R, Li J, et al. Graphitized carbon-coated vanadium carbide nanoboscages modified by nickel with enhanced electrocatalytic activity for hydrogen evolution in both acid and alkaline solutions. *J Mater Chem A* 2017;5(44):23028–34.
- [97] Xiong K, Li L, Zhang L, Ding W, Peng LS, Wang Y, et al. Ni-doped Mo_2C nanowires supported on Ni foam as a binder-free electrode for enhancing the hydrogen evolution performance. *J Mater Chem A* 2015;3(5):1863–7.
- [98] Xiong K, Huang LP, Gao Y, Zhang HD, Zhuo Y, Shen HZ, et al. Formation of a thin-layer of nickel hydroxide on nickel phosphide nanopillars for hydrogen evolution. *Electrochem Commun* 2018;92:9–13.
- [99] Cai WW, Yan L, Liang L, Xing W, Liu CP. Model-based design and optimization of the microscale mass transfer structure in the anode catalyst layer for direct methanol fuel cell. *AIChE J* 2013;59(3):780–6.
- [100] Takenaka S, Miyamoto H, Utsunomiya Y, Matsune H, Kishida M. Catalytic activity of highly durable Pt/CNT catalysts covered with hydrophobic silica layers for the oxygen reduction reaction in PEFCs. *J Phys Chem C* 2014;118(2):774–83.
- [101] Ji MB, Wei ZD, Chen SG, Li L. A novel antiflooding electrode for proton exchange membrane fuel cells. *J Phys Chem C* 2009;113(2):765–71.
- [102] Ji MB, Wei ZD, Chen SG, Zhang Q, Wang YQ, Qi XQ, et al. A more flooding-tolerant oxygen electrode in alkaline electrolyte. *Fuel Cells (Weinh)* 2010;10(2):289–98.
- [103] Wang MJ, Zhao T, Luo W, Mao ZX, Chen SG, Ding W, et al. Quantified mass transfer and superior antiflooding performance of ordered macroporous electrocatalysts. *AIChE J* 2018;64(7):2881–9.
- [104] Meng FL, Wang ZL, Zhong HX, Wang J, Yan JM, Zhang XB. Reactive multifunctional template-induced preparation of Fe-N-doped mesoporous carbon microspheres towards highly efficient electrocatalysts for oxygen reduction. *Adv Mater* 2016;28(36):7948–55.
- [105] Liang HW, Wei W, Wu ZS, Feng X, Müllen K. Mesoporous metal-nitrogen-doped carbon electrocatalysts for highly efficient oxygen reduction reaction. *J Am Chem Soc* 2013;135(43):16002–5.
- [106] Wei W, Liang H, Parvez K, Zhuang X, Feng X, Müllen K. Nitrogen-doped carbon nanosheets with size-defined mesopores as highly efficient metal-free catalyst for the oxygen reduction reaction. *Angew Chem Int Ed Engl* 2014;53(6):1570–4.

- [107] Lefèvre M, Proietti E, Jaouen F, Dodelet JP. Iron-based catalysts with improved oxygen reduction activity in polymer electrolyte fuel cells. *Science* 2009;324(5923):71–4.
- [108] Shui J, Chen C, Grabstanowicz L, Zhao D, Liu DJ. Highly efficient nonprecious metal catalyst prepared with metal-organic framework in a continuous carbon nanofibrous network. *Proc Natl Acad Sci USA* 2015;112(34):10629–34.
- [109] Meng Y, Voiry D, Goswami A, Zou X, Huang X, Chhowalla M, et al. N-, O-, and S-tridoped nanoporous carbons as selective catalysts for oxygen reduction and alcohol oxidation reactions. *J Am Chem Soc* 2014;136(39):13554–7.
- [110] Liu X, Zou S, Chen S. Ordered mesoporous carbons codoped with nitrogen and iron as effective catalysts for oxygen reduction reaction. *Nanoscale* 2016;8(46):19249–55.
- [111] Sun TT, Xu LB, Li SY, Chai WX, Huang Y, Yan YS, et al. Cobalt-nitrogen-doped ordered macro-/mesoporous carbon for highly efficient oxygen reduction reaction. *Appl Catal B* 2016;193:1–8.
- [112] Shen HJ, Gracia-Espino E, Ma JY, Tang HD, Mamat X, Wagberg T, et al. Atomically FeN₂ moieties dispersed on mesoporous carbon: a new atomic catalyst for efficient oxygen reduction catalysis. *Nano Energy* 2017;35:9–16.
- [113] Tan HB, Li YQ, Jiang XF, Tang J, Wang ZL, Qian HY, et al. Perfectly ordered mesoporous iron-nitrogen doped carbon as highly efficient catalyst for oxygen reduction reaction in both alkaline and acidic electrolytes. *Nano Energy* 2017;36:286–94.
- [114] Kong A, Dong B, Zhu X, Kong Y, Zhang J, Shan Y. Ordered mesoporous Porphyrin-like architectures as excellent cathode materials for the oxygen reduction reaction in both alkaline and acidic media. *Chem Eur J* 2013;19(48):16170–5.
- [115] Liang J, Du X, Gibson C, Du XW, Qiao SZ. N-doped graphene natively grown on hierarchical ordered porous carbon for enhanced oxygen reduction. *Adv Mater* 2013;25(43):6226–31.
- [116] Zhu C, Kim C, Aoki Y, Habazaki H. Nitrogen-doped hierarchical porous carbon architecture incorporated with cobalt nanoparticles and carbon nanotubes as efficient electrocatalyst for oxygen reduction reaction. *Adv Mater Interfaces* 2017;4(19):1700583.
- [117] Wei W, Ge HT, Huang LS, Kuang M, Al-Enizi AM, Zhang LJ, et al. Hierarchically tubular nitrogen-doped carbon structures for the oxygen reduction reaction. *J Mater Chem A* 2017;5(26):13634–8.
- [118] Liang HW, Zhuang X, Brüller S, Feng X, Müllen K. Hierarchically porous carbons with optimized nitrogen doping as highly active electrocatalysts for oxygen reduction. *Nat Commun* 2014;5(1):4973.
- [119] Ding W, Li L, Xiong K, Wang Y, Li W, Nie Y, et al. Shape fixing via salt recrystallization: a morphology-controlled approach to convert nano-structured polymer to carbon nanomaterial as a highly active catalyst for oxygen reduction reaction. *J Am Chem Soc* 2015;137(16):5414–20.
- [120] Wang W, Chen WH, Miao PY, Luo J, Wei ZD, Chen SL. NaCl crystallites as dual-functional and water-removable templates to synthesize a three-dimensional graphene-like macroporous Fe-N-C catalyst. *ACS Catal* 2017;7(9):6144–9.
- [121] Wang Y, Chen W, Nie Y, Peng L, Ding W, Chen S, et al. Construction of a porous nitrogen-doped carbon nanotube with open-ended channels to effectively utilize the active sites for excellent oxygen reduction reaction activity. *Chem Commun (Camb)* 2017;53(83):11426–9.
- [122] Wang Y, Chen W, Chen Y, Wei B, Chen LH, Peng LS, et al. Carbon-based catalysts by structural manipulation with iron for oxygen reduction reaction. *J Mater Chem A* 2018;6(18):8405–12.
- [123] Lim B, Jiang M, Tao J, Camargo PHC, Zhu Y, Xia Y. Shape-controlled synthesis of Pd nanocrystals in aqueous solutions. *Adv Funct Mater* 2009;19(2):189–200.
- [124] Xia Y, Xiong Y, Lim B, Skrabalak SE. Shape-controlled synthesis of metal nanocrystals: simple chemistry meets complex physics? *Angew Chem Int Ed Engl* 2009;48(1):60–103.
- [125] Pal J, Pal T. Faceted metal and metal oxide nanoparticles: design, fabrication and catalysis. *Nanoscale* 2015;7(34):14159–90.
- [126] Strmcnik DS, Tripkovic DV, van der Vliet D, Chang KC, Komanicky V, You H, et al. Unique activity of platinum adislands in the CO electrooxidation reaction. *J Am Chem Soc* 2008;130(46):15332–9.
- [127] Marković NM, Grgur BN, Ross PN. Temperature-dependent hydrogen electrochemistry on platinum low-index single-crystal surfaces in acid solutions. *J Phys Chem B* 1997;101(27):5405–13.
- [128] Marković NM, Ross PN Jr. Surface science studies of model fuel cell electrocatalysts. *Surf Sci Rep* 2002;45(4–6):117–229.
- [129] Marković NM, Sarraf ST, Gasteiger HA, Ross PN Jr. Hydrogen electrochemistry on platinum low-index single-crystal surfaces in alkaline solution. *J Chem Soc, Faraday Trans* 1996;92(20):3719–25.
- [130] Strmcnik D, Uchimura M, Wang C, Subbaraman R, Danilovic N, Van der Vliet D, et al. Improving the hydrogen oxidation reaction rate by promotion of hydroxyl adsorption. *Nat Chem* 2013;5(4):300–6.
- [131] van der Niet MJ, den Dunnen A, Juurlink LB, Koper MT. Co-adsorption of O and H₂O on nanostructured platinum surfaces: does OH form at steps? *Angew Chem Int Ed Engl* 2010;49(37):6572–5.
- [132] Wagner FT, Moylan T. Identification of surface hydronium: coadsorption of hydrogen-fluoride and water on platinum (111). *Surf Sci* 1987;182(1–2):125–49.
- [133] Baumann P, Pirug G, Reuter D, Bonzel HP. UHV adsorption studies of K/H₂O on Pt(111) and O/CH₃COOH on Cu(110): orientation and intermediates. *Surf Sci* 1995;335:186–96.
- [134] Chang SC, Weaver MJ. In situ infrared spectroscopy at single-crystal metal electrodes: an emerging link between electrochemical and ultrahigh-vacuum surface science. *J Phys Chem* 1991;95(14):5391–400.
- [135] Henderson MA. The interaction of water with solid surfaces: fundamental aspects revisited. *Surf Sci Rep* 2002;46(1–8):1–308.
- [136] Li H, Li Y, Koper MT, Calle-Vallejo F. Bond-making and breaking between carbon, nitrogen, and oxygen in electrocatalysis. *J Am Chem Soc* 2014;136(44):15694–701.
- [137] van der Niet MJTC, Garcia-Araez N, Hernández J, Felii JM, Koper MTM. Water dissociation on well-defined platinum surfaces: the electrochemical perspective. *Catal Today* 2013;202:105–13.
- [138] Koper MT. Structure sensitivity and nanoscale effects in electrocatalysis. *Nanoscale* 2011;3(5):2054–73.
- [139] Calle-Vallejo F, Loffreda D, Koper MT, Sautet P. Introducing structural sensitivity into adsorption-energy scaling relations by means of coordination numbers. *Nat Chem* 2015;7(5):403–10.
- [140] Marković NM, Adžić RR, Cahan BD, Yeager EB. Structural effects in electrocatalysis: oxygen reduction on platinum low index single-crystal surfaces in perchloric acid solutions. *J Electroanal Chem (Lausanne Switz)* 1994;377(1–2):249–59.
- [141] Zelenay P, Gamboa-Aldeco M, Horányi G, Wieckowski A. Adsorption of anions on ultrathin metal deposits on single-crystal electrodes: part 3. Voltammetric and radiochemical study of bisulfate adsorption on Pt(111) and Pt(poly) electrodes containing silver adatoms. *J Electroanal Chem (Lausanne Switz)* 1993;357(1–2):307–26.
- [142] Varga K, Zelenay P, Wieckowski A. Adsorption of anions on ultra-thin metal deposits on single-crystal electrodes: II: voltammetric and radiochemical study of bisulfate adsorption on Pt(111) and Pt(poly) electrodes containing copper adatoms. *J Electroanal Chem (Lausanne Switz)* 1992;330(1–2):453–67.
- [143] Gamboa-Aldeco ME, Herrero E, Zelenay PS, Wieckowski A. Adsorption of bisulfate anion on a Pt(100) electrode: a comparison with Pt(111) and Pt(poly). *J Electroanal Chem (Lausanne Switz)* 1993;348(1–2):451–7.
- [144] Narayanan R, El-Sayed MA. Catalysis with transition metal nanoparticles in colloidal solution: nanoparticle shape dependence and stability. *J Phys Chem B* 2005;109(26):12663–76.
- [145] Wang C, Daimon H, Lee Y, Kim J, Sun S. Synthesis of monodisperse Pt nanocubes and their enhanced catalysis for oxygen reduction. *J Am Chem Soc* 2007;129(22):6974–5.
- [146] Wang C, Daimon H, Onodera T, Koda T, Sun S. A general approach to the size- and shape-controlled synthesis of platinum nanoparticles and their catalytic reduction of oxygen. *Angew Chem Int Ed Engl* 2008;47(19):3588–91.
- [147] Lee CT, Yang X, Vara M, Gilroy KD, Xia Y. Water-based synthesis of sub-10 nm Pt octahedra and their performance towards the oxygen reduction reaction. *ChemNanoMat* 2017;3(12):879–84.
- [148] Bu L, Shao Q, Pi Y, Yao J, Luo M, Lang J, et al. Coupled s-p-d exchange in facet-controlled Pd₃Pb tripods enhances oxygen reduction catalysis. *Chem* 2018;4(2):359–71.
- [149] Wang C, Sang X, Gamler JTL, Chen DP, Unocic RR, Skrabalak SE. Facet-dependent deposition of highly strained alloyed shells on intermetallic nanoparticles for enhanced electrocatalysis. *Nano Lett* 2017;17(9):5526–32.
- [150] Gocyla M, Kuehl S, Shviro M, Heyen H, Selve S, Dunin-Borkowski RE, et al. Shape stability of octahedral PtNi nanocatalysts for electrochemical oxygen reduction reaction studied by *in situ* transmission electron microscopy. *ACS Nano* 2018;12(6):5306–11.
- [151] Van Santen RA. Complementary structure sensitive and insensitive catalytic relationships. *Acc Chem Res* 2009;42(1):57–66.
- [152] Quan Z, Wang Y, Fang J. High-index faceted noble metal nanocrystals. *Acc Chem Res* 2013;46(2):191–202.
- [153] Zhang H, Jin M, Xia Y. Noble-metal nanocrystals with concave surfaces: synthesis and applications. *Angew Chem Int Ed Engl* 2012;51(31):7656–73.
- [154] Yu T, Kim DY, Zhang H, Xia Y. Platinum concave nanocubes with high-index facets and their enhanced activity for oxygen reduction reaction. *Angew Chem Int Ed Engl* 2011;50(12):2773–7.
- [155] Zhang ZC, Hui JF, Liu ZC, Zhang X, Zhuang J, Wang X. Glycine-mediated syntheses of Pt concave nanocubes with high-index *hk0* facets and their enhanced electrocatalytic activities. *Langmuir* 2012;28(42):14845–8.
- [156] Tian N, Zhou ZY, Sun SG, Ding Y, Wang ZL. Synthesis of tetrahedral platinum nanocrystals with high-index facets and high electro-oxidation activity. *Science* 2007;316(5825):732–5.
- [157] Ye W, Sun Z, Wang C, Ye M, Ren C, Long R, et al. Enhanced O₂ reduction on atomically thin Pt-based nanoshells by integrating surface facet, interfacial electronic, and substrate stabilization effects. *Nano Res* 2018;11(6):3313–26.
- [158] Luo S, Tang M, Shen PK, Ye S. Atomic-scale preparation of octopod nanoframes with high-index facets as highly active and stable catalysts. *Adv Mater* 2017;29(8):201601687.
- [159] Luo M, Sun Y, Zhang X, Qin Y, Li M, Li Y, et al. Stable high-index faceted Pt skin on zigzag-like PtFe nanowires enhances oxygen reduction catalysis. *Adv Mater* 2018;30(10):1705515.
- [160] Jang Y, Choi KH, Chung DY, Lee JE, Jung N, Sung YE. Self-assembled dendritic Pt nanostructure with high-index facets as highly active and durable electrocatalyst for oxygen reduction. *ChemSusChem* 2017;10(15):3063–8.
- [161] Han XP, He GW, He Y, Zhang JF, Zheng XR, Li LL, et al. Engineering catalytic active sites on cobalt oxide surface for enhanced oxygen electrocatalysis. *Adv Energy Mater* 2018;8(10):1702222.

- [162] Wang H, Xie Y, Cao H, Li Y, Li L, Xu Z, et al. Flower-like nickel phosphide microballs assembled by nanoplates with exposed high-energy (001) facets: efficient electrocatalyst for the hydrogen evolution reaction. *ChemSusChem* 2017;10(24):4899–908.
- [163] Feng LL, Yu G, Wu Y, Li GD, Li H, Sun Y, et al. High-index faceted Ni₃S₂ nanosheet arrays as highly active and ultrastable electrocatalysts for water splitting. *J Am Chem Soc* 2015;137(44):14023–6.
- [164] Gao R, Zhu J, Xiao X, Hu Z, Liu J, Liu X. Facet-dependent electrocatalytic performance of Co₃O₄ for rechargeable Li–O₂ battery. *J Phys Chem C* 2015;119(9):4516–23.
- [165] Ling T, Yan DY, Jiao Y, Wang H, Zheng Y, Zheng X, et al. Engineering surface atomic structure of single-crystal cobalt (III) oxide nanorods for superior electrocatalysis. *Nat Commun* 2016;7(1):12876.
- [166] Su D, Dou S, Wang G. Single crystalline Co₃O₄ nanocrystals exposed with different crystal planes for Li–O₂ batteries. *Sci Rep* 2014;4(1):5767.
- [167] Zhao Y, Jia X, Chen G, Shang L, Waterhouse GIN, Wu LZ, et al. Ultrafine NiO nanosheets stabilized by TiO₂ from monolayer NiTi-LDH precursors: an active water oxidation electrocatalyst. *J Am Chem Soc* 2016;138(20):6517–24.
- [168] Su D, Ford M, Wang G. Mesoporous NiO crystals with dominantly exposed 110 reactive facets for ultrafast lithium storage. *Sci Rep* 2012;2(1):924.
- [169] Lukowski MA, Daniel AS, Meng F, Forticaux A, Li L, Jin S. Enhanced hydrogen evolution catalysis from chemically exfoliated metallic MoS₂ nanosheets. *J Am Chem Soc* 2013;135(28):10274–7.
- [170] Voiry D, Yamaguchi H, Li J, Silva R, Alves DC, Fujita T, et al. Enhanced catalytic activity in strained chemically exfoliated WS₂ nanosheets for hydrogen evolution. *Nat Mater* 2013;12(9):850–5.
- [171] Wang H, Lu Z, Xu S, Kong D, Cha JJ, Zheng G, et al. Electrochemical tuning of vertically aligned MoS₂ nanofilms and its application in improving hydrogen evolution reaction. *Proc Natl Acad Sci USA* 2013;110(49):19701–6.
- [172] Ding Q, Meng F, English CR, Cabán-Acevedo M, Shearer MJ, Liang D, et al. Efficient photoelectrochemical hydrogen generation using heterostructures of Si and chemically exfoliated metallic MoS₂. *J Am Chem Soc* 2014;136(24):8504–7.
- [173] Lukowski MA, Daniel AS, English CR, Meng F, Forticaux A, Hamers RJ, et al. Highly active hydrogen evolution catalysis from metallic WS₂ nanosheets. *Energy Environ Sci* 2014;7(8):2608–13.
- [174] Luxa J, Mazánek V, Pumera M, Lazar P, Sedmidubský D, Callisti M, et al. 2H→1T phase engineering of layered tantalum disulfides in electrocatalysis: oxygen reduction reaction. *Chem Eur J* 2017;23(33):8082–91.
- [175] Voiry D, Salehi M, Silva R, Fujita T, Chen M, Asefa T, et al. Conducting MoS₂ nanosheets as catalysts for hydrogen evolution reaction. *Nano Lett* 2013;13(12):6222–7.
- [176] Wu G, Wang J, Ding W, Nie Y, Li L, Qi X, et al. A strategy to promote the electrocatalytic activity of spinels for oxygen reduction by structure reversal. *Angew Chem Int Ed Engl* 2016;55(4):1340–4.
- [177] Gong Y, Ding W, Li Z, Su R, Zhang X, Wang J, et al. Inverse spinel cobalt–iron oxide and N-doped graphene composite as an efficient and durable bifunctional catalyst for Li–O₂ batteries. *ACS Catal* 2018;8(5):4082–90.
- [178] Millet P. Water electrolysis for hydrogen generation. In: Liu RS, Zhang L, Sun XL, Liu HS, Zhang JJ, editors. *Electrochemical technologies for energy storage and conversion*. Weinheim: Wiley-VCH; 2012.
- [179] Karunakaran R, Coghlan C, Tung TT, Kabiri S, Tran DNH, Doonan CJ, et al. Study of iron oxide nanoparticle phases in graphene aerogels for oxygen reduction reaction. *New J Chem* 2017;41(24):15180–6.
- [180] Yao W, Jing L, Wei ZD. Transition–metal–oxide based catalysts for oxygen reduction reaction. *J Mater Chem A* 2018;6(18):8194–209.
- [181] Liu Y, Xiao C, Lyu M, Lin Y, Cai W, Huang P, et al. Ultrathin Co₃S₄ nanosheets that synergistically engineer spin states and exposed polyhedra that promote water oxidation under neutral conditions. *Angew Chem Int Ed Engl* 2015;54(38):11231–5.
- [182] Suntivich J, Gasteiger HA, Yabuuchi N, Nakanishi H, Goodenough JB, Shao-Horn Y. Design principles for oxygen-reduction activity on perovskite oxide catalysts for fuel cells and metal–air batteries. *Nat Chem* 2011;3(7):546–50.
- [183] Wei C, Feng Z, Scherer GG, Barber J, Shao-Horn Y, Xu ZJ. Cations in octahedral sites: a descriptor for oxygen electrocatalysis on transition-metal spinels. *Adv Mater* 2017;29(23):1606800.
- [184] Smith RD, Prévot MS, Fagan RD, Trudel S, Berlinguette CP. Water oxidation catalysis: electrocatalytic response to metal stoichiometry in amorphous metal oxide films containing iron, cobalt, and nickel. *J Am Chem Soc* 2013;135(31):11580–6.
- [185] Smith RD, Prévot MS, Fagan RD, Zhang Z, Sedach PA, Siu MK, et al. Photochemical route for accessing amorphous metal oxide materials for water oxidation catalysis. *Science* 2013;340(6128):60–3.
- [186] Kuai L, Geng J, Chen C, Kan E, Liu Y, Wang Q, et al. A reliable aerosol-spray-assisted approach to produce and optimize amorphous metal oxide catalysts for electrochemical water splitting. *Angew Chem Int Ed Engl* 2014;53(29):7547–51.
- [187] Yang JS, Xu JJ. Nanoporous amorphous manganese oxide as electrocatalyst for oxygen reduction in alkaline solutions. *Electrochem Commun* 2003;5(4):306–11.
- [188] Indra A, Menezes PW, Sahraie NR, Bergmann A, Das C, Tallarida M, et al. Unification of catalytic water oxidation and oxygen reduction reactions: amorphous beat crystalline cobalt iron oxides. *J Am Chem Soc* 2014;136(50):17530–6.
- [189] Bergmann A, Martinez-Moreno E, Teschner D, Chernev P, Glied M, de Araújo JF, et al. Reversible amorphization and the catalytically active state of crystalline Co₃O₄ during oxygen evolution. *Nat Commun* 2015;6(1):8625.
- [190] Weber T, Mujsers JC, Niemantsverdriet JW. Structure of amorphous MoS₃. *J Phys Chem* 1995;99(22):9194–200.
- [191] Merki D, Fierro S, Vrabel H, Hu XL. Amorphous molybdenum sulfide films as catalysts for electrochemical hydrogen production in water. *Chem Sci (Camb)* 2011;2(7):1262–7.
- [192] Benck JD, Chen ZB, Kuritzky LY, Forman AJ, Jaramillo TF. Amorphous molybdenum sulfide catalysts for electrochemical hydrogen production: insights into the origin of their catalytic activity. *ACS Catal* 2012;2(9):1916–23.
- [193] Morales-Guio CG, Hu X. Amorphous molybdenum sulfides as hydrogen evolution catalysts. *Acc Chem Res* 2014;47(8):2671–81.
- [194] Ting LRL, Deng YL, Ma L, Zhang YJ, Peterson AA, Yeo BS. Catalytic activities of sulfur atoms in amorphous molybdenum sulfide for the electrochemical hydrogen evolution reaction. *ACS Catal* 2016;6(2):861–7.
- [195] Li Y, Yu Y, Huang Y, Nielsen RA, Goddard III WA, Li Y, et al. Engineering the composition and crystallinity of molybdenum sulfide for high-performance electrocatalytic hydrogen evolution. *ACS Catal* 2015;5(1):448–55.
- [196] Li G, Zhang D, Qiao Q, Yu Y, Peterson D, Zafar A, et al. All the catalytic active sites of MoS₂ for hydrogen evolution. *J Am Chem Soc* 2016;138(51):16632–8.
- [197] Lee JS, Park GS, Lee HI, Kim ST, Cao R, Liu M, et al. Ketjenblack carbon supported amorphous manganese oxides nanowires as highly efficient electrocatalyst for oxygen reduction reaction in alkaline solutions. *Nano Lett* 2011;11(12):5362–6.
- [198] Laursen AB, Vesborg PC, Chorkendorff I. A high-porosity carbon molybdenum sulphide composite with enhanced electrochemical hydrogen evolution and stability. *Chem Commun (Camb)* 2013;49(43):4965–7.
- [199] Wang T, Zhuo J, Du K, Chen B, Zhu Z, Shao Y, et al. Electrochemically fabricated polypyrrole and MoS_x copolymer films as a highly active hydrogen evolution electrocatalyst. *Adv Mater* 2014;26(22):3761–6.
- [200] Li DJ, Maiti UN, Lim J, Choi DS, Lee WJ, Oh Y, et al. Molybdenum sulfide/N-doped CNT forest hybrid catalysts for high-performance hydrogen evolution reaction. *Nano Lett* 2014;14(3):1228–33.
- [201] Chang YH, Lin CT, Chen TY, Hsu CL, Lee YH, Zhang W, et al. Highly efficient electrocatalytic hydrogen production by MoS_x grown on graphene-protected 3D Ni foams. *Adv Mater* 2013;25(5):756–60.
- [202] Ge X, Chen L, Zhang L, Wen Y, Hirata A, Chen M. Nanoporous metal enhanced catalytic activities of amorphous molybdenum sulfide for high-efficiency hydrogen production. *Adv Mater* 2014;26(19):3100–4.
- [203] Xie J, Zhang H, Li S, Wang R, Sun X, Zhou M, et al. Defect-rich MoS₂ ultrathin nanosheets with additional active edge sites for enhanced electrocatalytic hydrogen evolution. *Adv Mater* 2013;25(40):5807–13.
- [204] Zhang G, Kirkman PM, Patel AN, Cuharuc AS, McKelvey K, Unwin PR. Molecular functionalization of graphite surfaces: basal plane versus step edge electrochemical activity. *J Am Chem Soc* 2014;136(32):11444–51.
- [205] Pei DN, Gong L, Zhang AY, Zhang X, Chen JJ, Mu Y, et al. Defective titanium dioxide single crystals exposed by high-energy 001 facets for efficient oxygen reduction. *Nat Commun* 2015;6(1):8696.
- [206] Asset T, Chattot R, Fontana M, Mercier-Guyon B, Job N, Dubau L, et al. A review on recent developments and prospects for the oxygen reduction reaction on hollow Pt-alloy nanoparticles. *ChemPhysChem* 2018;19(13):1552–67.
- [207] Halck NB, Petrykin V, Krtil P, Rossmel J. Beyond the volcano limitations in electrocatalysis–oxygen evolution reaction. *Phys Chem Chem Phys* 2014;16(27):13682–8.
- [208] Yang MQ, Wang J, Wu H, Ho GW. Noble metal-free nanocatalysts with vacancies for electrochemical water splitting. *Small* 2018;14(15):1703323.
- [209] Yan D, Li Y, Huo J, Chen R, Dai L, Wang S. Defect chemistry of nonprecious-metal electrocatalysts for oxygen reactions. *Adv Mater* 2017;29(48):1606459.
- [210] Cheng F, Shen J, Peng B, Pan Y, Tao Z, Chen J. Rapid room-temperature synthesis of nanocrystalline spinels as oxygen reduction and evolution electrocatalysts. *Nat Chem* 2011;3(1):79–84.
- [211] Ma TY, Zheng Y, Dai S, Jaroniec M, Qiao SZ. Mesoporous MnCo₂O₄ with abundant oxygen vacancy defects as high-performance oxygen reduction catalysts. *J Mater Chem A* 2014;2(23):8676–82.
- [212] Li L, Feng XH, Nie Y, Chen SG, Shi F, Xiong K, et al. Insight into the effect of oxygen vacancy concentration on the catalytic performance of MnO₂. *ACS Catal* 2015;5(8):4825–32.
- [213] Zhou X, Jiang J, Ding T, Zhang J, Pan B, Zuo J, et al. Fast colloidal synthesis of scalable Mo-rich hierarchical ultrathin MoSe_{2-x} nanosheets for high-performance hydrogen evolution. *Nanoscale* 2014;6(19):11046–51.
- [214] Woods JM, Jung Y, Xie Y, Liu W, Liu Y, Wang H, et al. One-step synthesis of MoS₂/WS₂ layered heterostructures and catalytic activity of defective transition metal dichalcogenide films. *ACS Nano* 2016;10(2):2004–9.
- [215] Wang Y, Li J, Wei Z. Recent progress of carbon-based materials in oxygen reduction reaction catalysis. *ChemElectroChem* 2018;5(14):1764–74.
- [216] Zheng Y, Jiao Y, Qiao SZ. Engineering of carbon-based electrocatalysts for emerging energy conversion: from fundamentality to functionality. *Adv Mater* 2015;27(36):5372–8.
- [217] Tang C, Zhang Q. Nanocarbon for oxygen reduction electrocatalysis: dopants, edges, and defects. *Adv Mater* 2017;29(13):1604103.

- [218] Jin H, Huang H, He Y, Feng X, Wang S, Dai L, et al. Graphene quantum dots supported by graphene nanoribbons with ultrahigh electrocatalytic performance for oxygen reduction. *J Am Chem Soc* 2015;137(24):7588–91.
- [219] Jiang Y, Yang L, Sun T, Zhao J, Lyu Z, Zhuo O, et al. Significant contribution of intrinsic carbon defects to oxygen reduction activity. *ACS Catal* 2015;5(11):6707–12.
- [220] Zhao HY, Sun CH, Jin Z, Wang DW, Yan XC, Chen ZG, et al. Carbon for the oxygen reduction reaction: a defect mechanism. *J Mater Chem A* 2015;3(22):11736–9.
- [221] Zhao XJ, Zou XQ, Yan XC, Brown CL, Chen ZG, Zhu GS, et al. Defect-driven oxygen reduction reaction (ORR) of carbon without any element doping. *Inorg Chem Front* 2016;3(3):417–21.
- [222] Jia Y, Zhang L, Du A, Gao G, Chen J, Yan X, et al. Defect graphene as a trifunctional catalyst for electrochemical reactions. *Adv Mater* 2016;28(43):9532–8.
- [223] Tang C, Zhang R, Lu W, He L, Jiang X, Asiri AM, et al. Fe-doped CoP nanoarray: a monolithic multifunctional catalyst for highly efficient hydrogen generation. *Adv Mater* 2017;29(2):1602441.
- [224] Zhang X, Zhang X, Xu HM, Wu ZS, Wang HL, Liang YY. Iron-doped cobalt monophosphide nanosheet/carbon nanotube hybrids as active and stable electrocatalysts for water splitting. *Adv Funct Mater* 2017;27(24):1606635.
- [225] Liu TT, Liu DN, Qu FL, Wang DX, Zhang L, Ge RX, et al. Enhanced electrocatalysis for energy-efficient hydrogen production over CoP catalyst with nonelectroactive Zn as a promoter. *Adv Energy Mater* 2017;7(15):1700020.
- [226] Lin HL, Liu N, Shi ZP, Guo YL, Tang Y, Gao QS. Cobalt-doping in molybdenum-carbide nanowires toward efficient electrocatalytic hydrogen evolution. *Adv Funct Mater* 2016;26(31):5590–8.
- [227] Pan Y, Liu Y, Lin Y, Liu C. Metal doping effect of the M-Co₂P/nitrogen-doped carbon nanotubes (M = Fe, Ni, Cu) hydrogen evolution hybrid catalysts. *ACS Appl Mater Interfaces* 2016;8(22):13890–901.
- [228] Ji D, Peng LS, Shen JJ, Deng MM, Mao ZX, Tan LQ, et al. Inert V₂O₃ oxide promotes the electrocatalytic activity of Ni metal for alkaline hydrogen evolution. *Chem Comm* 2019;55(22):3290–3.
- [229] Liu T, Ma X, Liu D, Hao S, Du G, Ma Y, et al. Mn doping of CoP nanosheets array: an efficient electrocatalyst for hydrogen evolution reaction with enhanced activity at all pH values. *ACS Catal* 2017;7(1):98–102.
- [230] Wu K. Iron-doped cobalt phosphite nanoparticles as multifunctional hydrogen evolution catalyst. *Acta Phys Chim Sin* 2016;32(12):2819–20.
- [231] Xiao M, Wang SC, Thaweesak S, Luo B, Wang LZ. Tantalum (Oxy)nitride: narrow bandgap photocatalysts for solar hydrogen generation. *Engineering* 2017;3(3):365–78.
- [232] Zheng X, Peng L, Li L, Yang N, Yang Y, Li J, et al. Role of non-metallic atoms in enhancing the catalytic activity of nickel-based compounds for hydrogen evolution reaction. *Chem Sci (Camb)* 2018;9(7):1822–30.
- [233] Bonde J, Moses PG, Jaramillo TF, Nørskov JK, Chorkendorff I. Hydrogen evolution on nano-particulate transition metal sulfides. *Faraday Discuss* 2008;140:219–31.
- [234] Zhang K, Kim HJ, Lee JT, Chang GW, Shi X, Kim W, et al. Unconventional pore and defect generation in molybdenum disulfide: application in high-rate lithium-ion batteries and the hydrogen evolution reaction. *ChemSusChem* 2014;7(9):2489–95.
- [235] Lv XJ, She GW, Zhou SX, Li YM. Highly efficient electrocatalytic hydrogen production by nickel promoted molybdenum sulfide microspheres catalysts. *RSC Adv* 2013;3(44):21231–6.
- [236] Sun X, Dai J, Guo Y, Wu C, Hu F, Zhao J, et al. Semimetallic molybdenum disulfide ultrathin nanosheets as an efficient electrocatalyst for hydrogen evolution. *Nanoscale* 2014;6(14):8359–67.
- [237] Wang HT, Tsai C, Kong DS, Chan K, Abild-Pedersen F, Nørskov JK, et al. Transition-metal doped edge sites in vertically aligned MoS₂ catalysts for enhanced hydrogen evolution. *Nano Res* 2015;8(2):566–75.
- [238] Xie J, Zhang J, Li S, Grote F, Zhang X, Zhang H, et al. Controllable disorder engineering in oxygen-incorporated MoS₂ ultrathin nanosheets for efficient hydrogen evolution. *J Am Chem Soc* 2013;135(47):17881–8.
- [239] Zhang L, Wang XY, Zheng XQ, Peng LS, Shen JJ, Xiang R, et al. Oxygen-incorporated NiMoP₂ nanowire arrays for enhanced hydrogen evolution activity in alkaline solution. *ACS Appl Energy Mater* 2018;1(10):5482–9.
- [240] Duan JJ, Chen S, Jaroniec M, Qiao SZ. Heteroatom-doped graphene-based materials for energy-relevant electrocatalytic processes. *ACS Catal* 2015;5(9):5207–34.
- [241] Liu J, Song P, Ning ZG, Xu WL. Recent advances in heteroatom-doped metal-free electrocatalysts for highly efficient oxygen reduction reaction. *Electrocatalysis* 2015;6(2):132–47.
- [242] Zhang JT, Dai LM. Heteroatom-doped graphitic carbon catalysts for efficient electrocatalysis of oxygen reduction reaction. *ACS Catal* 2015;5(12):7244–53.
- [243] Cui H, Zhou Z, Jia D. Heteroatom-doped graphene as electrocatalysts for air cathodes. *Mater Horiz* 2017;4(1):7–19.
- [244] Zhou W, Jia J, Lu J, Yang L, Hou D, Li G, et al. Recent developments of carbon-based electrocatalysts for hydrogen evolution reaction. *Nano Energy* 2016;28:29–43.
- [245] Bayatsarmadi B, Zheng Y, Vasileff A, Qiao SZ. Recent advances in atomic metal doping of carbon-based nanomaterials for energy conversion. *Small* 2017;13(21):13.
- [246] Li R, Wei ZD, Gou XL, Xu W. Phosphorus-doped graphene nanosheets as efficient metal-free oxygen reduction electrocatalysts. *RSC Adv* 2013;3(25):9978–84.
- [247] Li R, Wei ZD, Gou XL. Nitrogen and phosphorus dual-doped graphene/carbon nanosheets as bifunctional electrocatalysts for oxygen reduction and evolution. *ACS Catal* 2015;5(7):4133–42.
- [248] Yang N, Li L, Li J, Ding W, Wei Z. Modulating the oxygen reduction activity of heteroatom-doped carbon catalysts via the triple effect: charge, spin density and ligand effect. *Chem Sci (Camb)* 2018;9(26):5795–804.
- [249] Wang H, Yang N, Li W, Ding W, Chen K, Li J, et al. Understanding the roles of nitrogen configurations in hydrogen evolution: trace atomic cobalt boosts the activity of planar nitrogen-doped graphene. *ACS Energy Lett* 2018;3(6):1345–52.
- [250] Zhang ZC, Xu B, Wang X. Engineering nanointerfaces for nanocatalysis. *Chem Soc Rev* 2014;43(22):7870–86.
- [251] Shi J. On the synergetic catalytic effect in heterogeneous nanocomposite catalysts. *Chem Rev* 2013;113(3):2139–81.
- [252] Guo S, Zhang S, Sun S. Tuning nanoparticle catalysis for the oxygen reduction reaction. *Angew Chem Int Ed Engl* 2013;52(33):8526–44.
- [253] Wang KX, Li XH, Chen JS. Surface and interface engineering of electrode materials for lithium-ion batteries. *Adv Mater* 2015;27(3):527–45.
- [254] Liang YR, Zhang WC, Wu DC, Ni QQ, Zhang MQ. Interface engineering of carbon-based nanocomposites for advanced electrochemical energy storage. *Adv Mater Interfaces* 2018;5(14):1800430.
- [255] Dang K, Wang T, Li C, Zhang J, Liu S, Gong J. Improved oxygen evolution kinetics and surface states passivation of Ni-Bi Co-catalyst for a hematite photoanode. *Engineering* 2017;3(3):285–9.
- [256] Bai S, Xiong Y. Some recent developments in surface and interface design for photocatalytic and electrocatalytic hybrid structures. *Chem Commun (Camb)* 2015;51(51):10261–71.
- [257] Zhang J, Wang T, Liu P, Liao Z, Liu S, Zhuang X, et al. Efficient hydrogen production on MoNi₄ electrocatalysts with fast water dissociation kinetics. *Nat Commun* 2017;8(1):15437.
- [258] Xue ZH, Su H, Yu QY, Zhang B, Wang HH, Li XH, et al. Janus Co/CoP nanoparticles as efficient Mott-Schottky electrocatalysts for overall water splitting in wide pH range. *Adv Energy Mater* 2017;7(12):1602355.
- [259] Xu H, Shi ZX, Tong YX, Li GR. Porous microrod arrays constructed by carbon-confined NiCo@NiCo₂ core@shell nanocrystals as efficient electrocatalysts for oxygen evolution. *Adv Mater* 2018;30(21):1705442.
- [260] Hu L, Song XF, Zhang SL, Zeng HB, Zhang XJ, Marks R, et al. MoS₂ nanoparticles coupled to SnS₂ nanosheets: the structural and electronic modulation for synergetic electrocatalytic hydrogen evolution. *J Catal* 2018;366:8–15.
- [261] Zhou X, Liu Y, Ju H, Pan B, Zhu J, Ding T, et al. Design and epitaxial growth of MoSe₂-NiSe vertical heterostructures with electronic modulation for enhanced hydrogen evolution reaction. *Chem Mater* 2016;28(6):1838–46.
- [262] Zhao D, Pi Y, Shao Q, Feng Y, Zhang Y, Huang X. Enhancing oxygen evolution electrocatalysis via the intimate hydroxide-oxide interface. *ACS Nano* 2018;12(6):6245–51.
- [263] Yang J, Zhu G, Liu Y, Xia J, Ji Z, Shen X, et al. Fe₃O₄-decorated Co₉S₈ nanoparticles *in situ* grown on reduced graphene oxide: a new and efficient electrocatalyst for oxygen evolution reaction. *Adv Funct Mater* 2016;26(26):4712–21.
- [264] Zhao S, Jin R, Song Y, Zhang H, House SD, Yang JC, et al. Atomically precise gold nanoclusters accelerate hydrogen evolution over MoS₂ nanosheets: the dual interfacial effect. *Small* 2017;13(43):1701519.
- [265] Huang J, Su Y, Zhang Y, Wu W, Wu C, Sun Y, et al. FeO_x/FeP hybrid nanorods neutral hydrogen evolution electrocatalysis: insight into interface. *J Mater Chem A* 2018;6(20):9467–72.
- [266] Deng Z, Wang J, Nie Y, Wei Z. Tuning the interface of Ni@Ni(OH)₂/Pd/rGO catalyst to enhance hydrogen evolution activity and stability. *J Power Sources* 2017;352:26–33.
- [267] Kim M, Kim S, Song D, Oh S, Chang KJ, Cho E. Promotion of electrochemical oxygen evolution reaction by chemical coupling of cobalt to molybdenum carbide. *Appl Catal B* 2018;227:340–8.
- [268] Yu X, Zhao J, Zheng LR, Tong Y, Zhang M, Xu G, et al. Hydrogen evolution reaction in alkaline media: alpha- or beta-nickel hydroxide on the surface of platinum? *ACS Energy Lett* 2018;3(1):237–44.
- [269] Han X, Wu X, Deng Y, Liu J, Lu J, Zhong C, et al. Ultrafine Pt nanoparticle-decorated pyrite-type CoS₂ nanosheet arrays coated on carbon cloth as a bifunctional electrode for overall water splitting. *Adv Energy Mater* 2018;8(24):1800935.
- [270] Peng L, Zheng X, Li L, Zhang L, Yang N, Xiong K, et al. Chimney effect of the interface in metal oxide/metal composite catalysts on the hydrogen evolution reaction. *Appl Catal B* 2019;245:122–9.
- [271] Peng L, Shen J, Zheng X, Xiang R, Deng M, Mao Z, et al. Rationally design of monometallic NiO-Ni₃S₂/NF heteronanosheets as bifunctional electrocatalysts for overall water splitting. *J Catal* 2019;369:345–51.
- [272] An L, Li Y, Luo M, Yin J, Zhao YQ, Xu C, et al. Atomic-level coupled interfaces and lattice distortion on CuS/NiS₂ nanocrystals boost oxygen catalysis for flexible Zn-air batteries. *Adv Funct Mater* 2017;27(42):1703779.
- [273] Liu J, Zheng Y, Zhu D, Vasileff A, Ling T, Qiao SZ. Identification of pH-dependent synergy on Ru/MoS₂ interface: a comparison of alkaline and acidic hydrogen evolution. *Nanoscale* 2017;9(43):16616–21.
- [274] Guo K, Zou Z, Du J, Zhao Y, Zhou B, Xu C. Coupling FeSe₂ with CoSe: an effective strategy to create stable and efficient electrocatalysts for water oxidation. *Chem Commun (Camb)* 2018;54(79):11140–3.

- [275] Ni B, He P, Liao W, Chen S, Gu L, Gong Y, et al. Surface oxidation of AuNi heterodimers to achieve high activities toward hydrogen/oxygen evolution and oxygen reduction reactions. *Small* 2018;14(14):1703749.
- [276] Zhu C, Wang AL, Xiao W, Chao D, Zhang X, Tiej NH, et al. *In situ* grown epitaxial heterojunction exhibits high-performance electrocatalytic water splitting. *Adv Mater* 2018;30(13):1705516.
- [277] Huang J, Sun Y, Du X, Zhang Y, Wu C, Yan C, et al. Cytomembrane-structure-inspired active Ni-N-O interface for enhanced oxygen evolution reaction. *Adv Mater* 2018;30(39):1803367.
- [278] Li Y, Yin J, An L, Lu M, Sun K, Zhao YQ, et al. FeS₂/CoS₂ interface nanosheets as efficient bifunctional electrocatalyst for overall water splitting. *Small* 2018;14(26):1801070.
- [279] Gao W, Xia Z, Cao F, Ho JC, Jiang Z, Qu Y. Comprehensive understanding of the spatial configurations of CeO₂ in NiO for the electrocatalytic oxygen evolution reaction: embedded or surface-loaded. *Adv Funct Mater* 2018;28(11):1706056.
- [280] Hu W, Zhang Y, Song D, Wang Y. Amorphous Ni-Mo-Fe alloy as the electrode for hydrogen evolution reaction of alkaline water electrolysis. *J Funct Mater* 1995;5:456–8.
- [281] Han Q, Wei X, Liu K. Development of nickel alloys as HER cathodes for water electrolysis. *Chin J Nonferr Metal* 2001;11(z1):158–62. Chinese.
- [282] Peng X, Omasta TJ, Roller JM, Mustain WE. Highly active and durable Pd-Cu catalysts for oxygen reduction in alkaline exchange membrane fuel cells. *Front Energy* 2017;11(3):299–309.
- [283] Chang QW, Xu Y, Zhu SQ, Xiao F, Shao MH. Pt-Ni nanourchins as electrocatalysts for oxygen reduction reaction. *Front Energy* 2017;11(3):254–9.
- [284] Wang Z, Ren X, Luo Y, Wang L, Cui G, Xie F, et al. An ultrafine platinum-cobalt alloy decorated cobalt nanowire array with superb activity toward alkaline hydrogen evolution. *Nanoscale* 2018;10(26):12302–7.
- [285] Jakšić MM. Electrocatalysis of hydrogen evolution in the light of the brewerengel theory for bonding in metals and intermetallic phases. *Electrochim Acta* 1984;29(11):1539–50.
- [286] Raj IA. Nickel-based, binary-composite electrocatalysts for the cathodes in the energy-efficient industrial-production of hydrogen from alkaline-water electrolytic cells. *J Mater Sci* 1993;28(16):4375–82.
- [287] Zhang L, Xiong K, Nie Y, Wang XX, Liao JH, Wei ZD. Sputtering nickel-molybdenum nanorods as an excellent hydrogen evolution reaction catalyst. *J Power Sources* 2015;297:413–8.
- [288] Bing Y, Liu H, Zhang L, Ghosh D, Zhang J. Nanostructured Pt-alloy electrocatalysts for PEM fuel cell oxygen reduction reaction. *Chem Soc Rev* 2010;39(6):2184–202.
- [289] Antolini E, Salgado JRC, Gonzalez ER. The stability of Pt–M (M = first row transition metal) alloy catalysts and its effect on the activity in low temperature fuel cells: a literature review and tests on a Pt–Co catalyst. *J Power Sources* 2006;160(2):957–68.
- [290] Mukerjee S, Srinivasan S. Enhanced electrocatalysis of oxygen reduction on platinum alloys in proton-exchange membrane fuel-cells. *J Electroanal Chem (Lausanne Switz)* 1993;357(1–2):201–24.
- [291] Colón-Mercado HR, Popov BN. Stability of platinum based alloy cathode catalysts in PEM fuel cells. *J Power Sources* 2006;155(2):253–63.
- [292] Murthi VS, Izzo E, Bi W, Guerrero S, Protsailo L. Highly dispersed alloy catalyst for durability. South Windsor: UTC power Corporation; 2013.
- [293] Greeley J, Stephens IE, Bondarenko AS, Johansson TP, Hansen HA, Jaramillo TF, et al. Alloys of platinum and early transition metals as oxygen reduction electrocatalysts. *Nat Chem* 2009;1(7):552–6.
- [294] Bamos G, Bebelis S, Kondarides DI, Verykios X. Comparison of the activity of Pd–M (M: Ag, Co, Cu, Fe, Ni, Zn) bimetallic electrocatalysts for oxygen reduction reaction. *Top Catal* 2017;60(15–16):1260–73.
- [295] Faber MS, Lukowski MA, Ding Q, Kaiser NS, Jin S. Earth-abundant metal pyrites (FeS₂, CoS₂, NiS₂, and their alloys) for highly efficient hydrogen evolution and polysulfide reduction electrocatalysis. *J Phys Chem C* 2014;118(37):21347–56.
- [296] Kiran V, Mukherjee D, Jenjeti RN, Sampath S. Active guests in the MoS₂/MoSe₂ host lattice: efficient hydrogen evolution using few-layer alloys of MoS₂(1–x)Se_{2x}. *Nanoscale* 2014;6(21):12856–63.
- [297] Xu C, Peng S, Tan C, Ang H, Tan H, Zhang H, et al. Ultrathin S-doped nanosheets for efficient hydrogen evolution. *J Mater Chem A* 2014;2(16):5597–601.
- [298] Xu K, Wang F, Wang Z, Zhan X, Wang Q, Cheng Z, et al. Component-controllable WS₂(1–x)Se_{2x} nanotubes for efficient hydrogen evolution reaction. *ACS Nano* 2014;8(8):8468–76.
- [299] Gong Q, Cheng L, Liu C, Zhang M, Feng Q, Ye H, et al. Ultrathin MoS₂(1–x)Se_{2x} alloy nanoflakes for electrocatalytic hydrogen evolution reaction. *ACS Catal* 2015;5(4):2213–9.
- [300] Cabán-Acevedo M, Stone ML, Schmidt JR, Thomas JG, Ding Q, Chang HC, et al. Efficient hydrogen evolution catalysis using ternary pyrite-type cobalt phosphosulphide. *Nat Mater* 2015;14(12):1245–51.